

LIBRARIES MICHIGAN STATE UNIVERSITY EAST LANSING, MICH 48824-1048

0000 62220975

This is to certify that the thesis entitled

COMPUTATIONAL INVESTIGATON OF THE VANELSEE DIFFUSER FLOW FIELD

presented by

TOSHIYUKI SATO

has been accepted towards fulfillment of the requirements for the

M.S. degree in Mechanical Engineering

Major Professor's Signature

OS 22 0 0

Date

MSU is an Affirmative Action/Equal Opportunity Institution

PLACE IN RETURN BOX to remove this checkout from your record. TO AVOID FINES return on or before date due. MAY BE RECALLED with earlier due date if requested.

<u>DATE DUE</u>	<u>DATE DUE</u>	<u>DATE DUE</u>

6/01 c:/CIRC/DateDue.p65-p.15

COMPUTATIONAL INVESTIGATION OF THE VANELESS DIFFUSER FLOW FIELD

By

Toshiyuki Sato

A THESIS

Submitted to
Michigan State University
in partial fulfillment of the requirements
for the degree of

MASTER OF SCIENCE

Department of Mechanical Engineering

2004

ABSTRACT

COMPUTATIONAL INVESTIGATION OF THE VANELESS DIFFUSER FLOW FIELD

By

Toshiyuki Sato

The fluid leaving a centrifugal compressor impeller contains a high amount of kinetic energy to a diffuser. Downstream of the impeller, in the diffuser, part of this energy is diffused and transformed to static pressure. In this present work, the Vaneless Diffuser is used. An existing experimental data of a vaneless diffuser was numerically verified, using Computational Fluid Dynamics (CFD). In order to improve the compressor performance, it is necessary to understand the detailed flow pattern in the diffuser.

The flow in the vanless diffuser was numerically analyzed and the result compared with the experimental data. The computation was carried out by applying the experimental data as an initial input just after the impeller and corresponding boundary conditions.

The main objective of this study was to verify the numerical accuracy and contribute knowledge towards predicting the performance of the compressor theoretically, which is very essential for the compressor designer and user.



TABLE OF CONTENTS

	page
LIST OF FIGURES	v
LIST OF SYMBOLS	ix
CHAPTER 1	
INTRODUCTION OF CENTRIFUGAL COMPRESSORS AND DIFFUSERS	31
1-1. Introduction	1
1-2. Geometrical Effects	6
CHAPTER 2	
PROCEDURES	9
2-1. Introduction	9
2-2. Geometry and Grid	9
2-3. Boundary Conditions	10
2-3-1. Inlet Boundary Conditions	10
2-3-2. Axisymmetric Swirl Flows	13
2-3-3. The Turbulent Model: Spalart-Allmaras Model	13
CHAPTER 3	
RESULTS AND DISCUSSION	16
3-1. Comparative Analysis	16
3-1-1. Flow Velocities	17
3-1-2. Contours	19
3-2. Predictive Analysis	20
CHAPTER4	
CONCLUSIONS AND FUTURE WORK	22
4. Conclusions and Future Work	22
BIBLIOGRAPHY	24
FIGURES	27

LIST OF FIGURES

Figure 1-1 Vaneless Diffuser	Page ⊿
Figure 1-2 Centrifugal Compressor	
Figure 2 (A) Schematic Layout of Vaneless Diffuser – Geometry & Grid (mm).	8
Figure 2 (B) Computational Grid – Geometry & Grid (mm)	8
Figure 3 (A) Swirl Velocity Cu (m/s) – Inlet Velocity Profiles	12
Figure 3 (B) Radial Velocity Cr (m/s) – Inlet Velocity Profiles	12
Figure 4-1 Absolute Radial and Swirl Velocity (Cr/U ₂ , Cu/U ₂) – C.F.D vs. Experiment, n=13000 rpm	28
Figure 4-2 Total Pressure and Total Temperature (π , τ) – C.F.D vs. Experiment, n=13000 rpm	30
Figure 4-3 Flow Angle (α) – C.F.D vs. Experiment, n=13000 rpm	32
Figure 5-1 Absolute Radial and Swirl Velocity (Cr/U ₂ , Cu/U ₂) – C.F.D vs. Experiment, n=15500 rpm	34
Figure 5-2 Total Pressure and Total Temperature (π, τ) – C.F.D vs. Experiment, n=15500 rpm	36
Figure 5-3 Flow Angle (α) – C.F.D vs. Experiment, n=15500 rpm	38
Figure 6-1 Absolute Radial and Swirl Velocity (Cr/U ₂ , Cu/U ₂)	
C.F.D vs. Experiment, n=18000 rpm	40
Figure 6-2 Total Pressure and Total Temperature (π , τ) – C.F.D vs. Experiment, n=18000 rpm	42

Figure 6-3 Flow Angle (α) – C.F.D vs. Experiment, n=18000 rpm	44
Figure 7-1 Absolute Radial and Swirl Velocity (Cr/U ₂ , Cu/U ₂) – C.F.D vs. Experiment, n=20500 rpm	46
Figure 7-2 Total Pressure and Total Temperature (π, τ) – C.F.D vs. Experiment, n=20500 rpm	48
Figure 7-3 Flow Angle (α) – C.F.D vs. Experiment, n=20500 rpm	49
Figure 8-1 Contours of Flow Angle (α , 13000 rpm)	52
Figure 8-2 Contours of Absolute Radial Velocity (Cr/U ₂ , 13000 rpm)	52
Figure 8-3 Contours of Total Pressure $(\pi, 13000 \text{ rpm})$	53
Figure 8-4 Contours of Absolute Swirl Velocity (Cu/U ₂ , 13000 rpm)	53
Figure 8-5 Contours of Velocity Magnitude (m/s), 13000 rpm	54
Figure 8-6 Velocity Vectors Colored by Velocity Magnitude, 13000 rpm	54
Figure 8-7 Contours of Total Temperature (K), 13000 rpm	55
Figure 9-1 Contours of Flow Angle (α , 15500 rpm)	56
Figure 9-2 Contours of Absolute Radial Velocity (Cr/U ₂ , 15500 rpm)	56
Figure 9-3 Contours of Total Pressure $(\pi, 15500 \text{ rpm})$	57
Figure 9-4 Contours of Absolute Swirl Velocity (Cu/U ₂ , 15500 rpm)	57
Figure 9-5 Contours of Velocity Magnitude (m/s), 15500 rpm	58
Figure 9-6 Velocity Vectors Colored by Velocity Magnitude, 15500 rpm	58

Figure 9-7 Contours of Total Temperature (K), 15500 rpm	59
Figure 10-1 Contours of Flow Angle ($lpha$, 18000 rpm)	60
Figure 10-2 Contours of Absolute Radial Velocity (Cr/U ₂ , 18000 rpm)	60
Figure 10-3 Contours of Total Pressure (π, 18000 rpm)	61
Figure 10-4 Contours of Absolute Swirl Velocity (Cu/U ₂ , 18000 rpm)	61
Figure 10-5 Contours of Velocity Magnitude (m/s), 18000 rpm	62
Figure 10-6 Velocity Vectors Colored by Velocity Magnitude, 18000 rpm	62
Figure 10-7 Contours of Total Temperature (K), 18000 rpm	63
Figure 11-1 Contours of Flow Angle ($lpha$, 20500 rpm)	64
Figure 11-2 Contours of Absolute Radial Velocity (Cr/U ₂ , 20500 rpm)	64
Figure 11-3 Contours of Total Pressure (π, 20500 rpm)	65
Figure 11-4 Contours of Absolute Swirl Velocity (Cu/U ₂ , 20500 rpm)	65
Figure 11-5 Contours of Velocity Magnitude (m/s), 20500 rpm	66
Figure 11-6 Velocity Vectors Colored by Velocity Magnitude, 20500 rpm	66
Figure 11-7 Contours of Total Temperature (K), 20500 rpm	67
Figure 12 Inlet Velocity Prediction (Cr & Cu)	68
Figure 13 Prediction of Boundary Conditions, Flow Angle ($lpha$)	69
Figure 14 Prediction of Boundary Conditions, Total Pressure (Pa)	70

Figure	15 Prediction of Boundary Conditions, Radial Velocity Cr (m/s)	71
Figure	16 Prediction of Boundary Conditions, Swirl Velocity Cu (m/s)	72
Figure	17 Prediction of Boundary Conditions, Velocity Magnitude (m/s)	73
Figure	15 Prediction of Boundary Conditions, Path Line	74

LIST OF SYMBOLS

NOTATION

- b Diffuser inlet height (mm)
- D Diameter (mm)
- h Height (mm)
- n Rotational speed (rpm)
- π Total pressure
- au Total temperature
- α Flow angle (degree)
- C Velocity (m/s)
- U Impeller speed (m/s)

Subscripts

- 2 Inlet of diffuser
- 3 Outlet of diffuser
- r Radial
- u Swirl/Rotational

CHAPTER 1

INTRODUCTION OF CETRIFUGAL COMPRESSORS AND DIFFUSERS

1-1. INTRODUCTION

Figure 1.2 shows that a centrifugal compressor consists of two parts, which are an impeller and a diffuser. The diffuser may lead pressurized fluid to the exit pipe system. The energy is transferred to the fluid in the impeller, and then the fluid leaves the impeller with a high amount of kinetic energy. To achieve a good efficiency, it is necessary to convert the kinetic energy to static pressure rise smoothly. To change the kinetic energy to static pressure rise, two different methods can be used:

- > Increasing the flow area, which reduces the velocity and increases the static pressure
- > Changing the mean flow path radius, which decreases the tangential velocity and increases the static pressure

The diffusers of centrifugal compressor can be of two different types, which are vaneless and vaned. Vaneless diffusers are used when large operation range and inexpensive design are primary goals. On the other hand, the vaned diffuser has a more limited operation range and more complex geometry, which means more expensive design.

In this study, all of experimental data was supplied by Turbomachinery Laboratory, Michigan State University. On the other hand, the computational fluid dynamics (CFD) is used to investigate the flow field of the diffuser, numerically. And the experimental data was used as the input boundary condition for this computation. The goals of this study are:

- > To study steady phenomena in the vaneless diffuser with CFD
- > To study the effect of input conditions change with CFD
- > To compare with the experimental data and the numerical data
- > To predict inlet boundary conditions and make sure the effects and accuracy

The diffusers of centrifugal compressors have been studied for many

decades, and comprehensive literature on the design and construction of different kinds of diffusers is available.

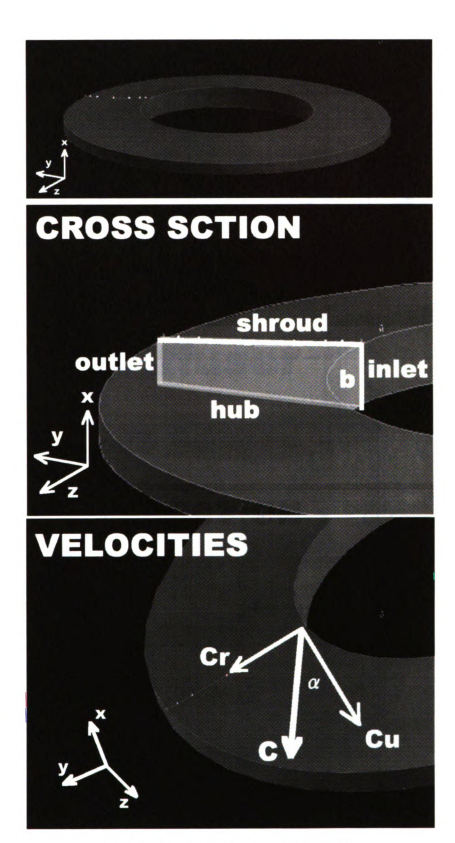


Figure 1-1: VANELESS DIFFUSER

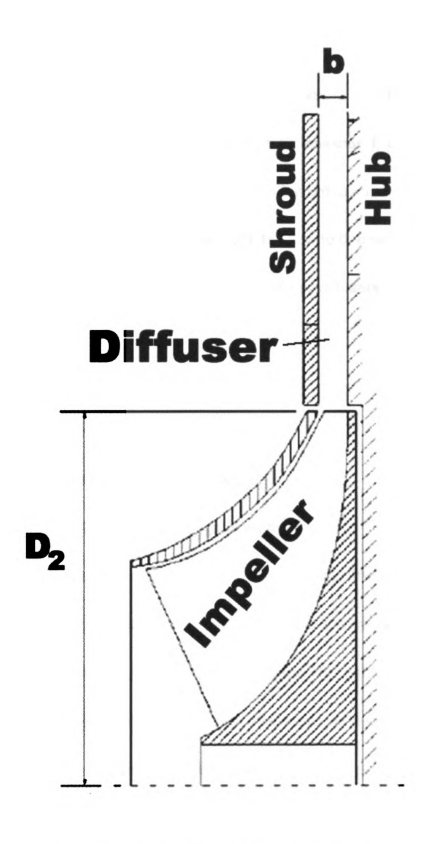


Figure 1-2: CENTRIFUGAL COMPRESSOR

5

1-2. GEOMETRICAL EFFECTS

The geometry of the vaneless diffuser is very simple. It consists of parallel or almost parallel walls which form a radial annular passage from the impeller outlet radius to some outlet radius of the diffuser. The diffuser is usually followed by a volute or a collecting chamber which leads the flow to one single exit.

Ludtke (1983) has tested four types of vaneless diffusers:

- > parallel walls
- highly tapered
- > constant area
- > parallel walls but reduced width

(reduced 52.7% from the original width)

The diffuser with the parallel walls showed best efficiency. The diffuser with the constant area diffuser has a slightly lower efficiency but the operation range was larger. The narrowed diffuser decreased the efficiency. The highly tapered diffuser showed improvement in surge margin but the efficiency was decreased.

Yingkang and Sjolander (1987) have tested vaneless diffusers with various taper angles. They found that small amount of wall convergence was beneficial and yielded better static pressure recovery at the intermediate flow rate

than parallel wall diffuser. The parallel wall diffuser showed better static pressure recovery at the high flow rate.

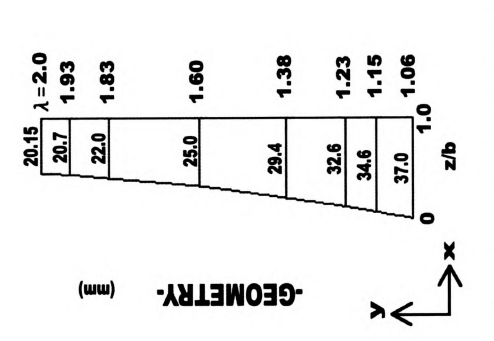
Liberti et al. (1996) have tested two vaneless diffusers with different widths. They found that a narrower diffuser showed better efficiency and total-total pressure ratio than a wider diffuser.

Japikse and Baines (1998) have found that the aspect ratio, AS=b/W₁, was strongly coupled with aerodynamic blockage, Mack number, and Reynolds number. Small aspect ratios invariably penalize the pressure recovery substantially. Large area ratios are usually less deleterious, but the variations must be carefully considered.

The walls of the vaneless diffuser are usually straight. Lee et al. (2001) have optimized the vaneless diffuser of the centrifugal compress using the Direct Method of Optimization (DMO). In their optimization method the height of the diffuser was altered by moving the shroud wall. They optimized the new geometry which had a minimum height at the middle of the diffuser passage. it showed 2-3% increase of efficiency at the design point and 1-5% increase of efficiency at the off-design point.



-GRID-



(A) Schematic Layout of Vaneless Diffuser

Figure 2: GEOMETRY & GRID (mm)

(B) Computational Grid

CHAPTER 2

PROCEDURES

2-1. INTRODUCTION

In this study, performance of a vaneless diffuser was investigated using a computational fluid dynamics (CFD) analysis. Also numerical simulations were done to analyze further details. All of the experimental data was supplied by Turbomachinary Laboratory Michigan State University. The flow solver *Fluent* v.6 was used to solve the flow field. The solver is capable to solve compressible, incompressible, steady, and steady flow fields. *Spalart-Allmaras turbulence model* was used in this analysis. As the inlet boundary condition, *Turbulence Specification Method* was used and the value of *Modified Turbulent Viscosity* was set up as 0.05. *Axisymmetric Swirl* was applied for the space to simulate the swirl velocity as a symmetry velocity along the x-axis using two-dimensional grid.

2-2. GEOMETRY AND GRID

The schematic geometry and the computational grid are shown in Figure 2 respectively. The diffuser is simple vaneless diffuser. The inlet diameter: D₂ is

290 (mm) and the exit diameter: D_3 is 580 (mm). The heights of each point are shown as above. The passage of the diffuser through the inlet to outlet was divided into nine parts, $\lambda = d/D_2$; 1.06, 1.15, 1.23, 1.38, 1.60 1.83, and 1.93. "z/b" means the distance toward the shroud from the hub at the diffuser inlet.

Figure 2(A) presents the two dimensional computational grid created with the interactive grid generator *Gambit, Fluent Inc.* The number of cells is 6525.

Axisymmetric Swirl was applied to the grid to compute the swirl velocities.

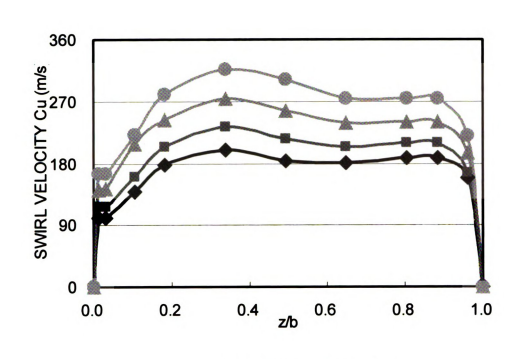
2-3. BOUNDARY CONDITIONS

2-3-1. INLET BOUNDARY CONDITIONS

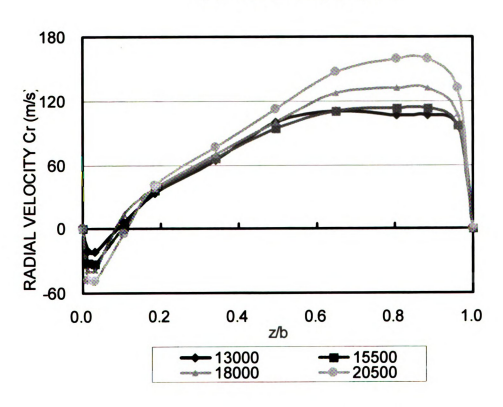
The experimental data was used for the inlet boundary conditions. The radius velocity Cr, and the swirl velocity Cu, which were from the experimental data, were read very carefully, and then put directly into the inlet boundary conditions. Also the temperature data was used as the inlet boundary. Pressure was not applied as inlet boundary conditions, but gage pressure was applied to entire flow filed.

Figure 3 shows the radial and swirl velocities of each rotational speed which were used for the inlet boundary conditions. Figure 3(A) shows that the

swirl velocities simply become bigger in proportion to the rotational speed. And Figure 3(B) presents that when the rotational speed is getting bigger and bigger, the reverse flow at the inlet shroud side is getting stronger.



(A) Swirl Velocity Cu (m/s)



(B) Radial Velocity Cr (m/s)

Figure 3: INLET VELOCITY PROFILES

2-3-2. AXISYMMETRIC SWIRL FLOWS

Axisymmetric Swirl was applied for the computational grid. In this vaneless diffuser case, axial (tangential) velocities are not important. And with this two dimensional grid, it is impossible to calculate the swirl velocities. But Axisymmetric Swirl may lead to indicate the swirling velocities Cu. The difficulties associated with solving swirling and rotating velocities are a result of the high degree of coupling between the momentum equations, which is introduced when the influence of the rotational terms is large. A high level of rotation introduces a large radial pressure gradient which drives the flow in the axial and radial directions. This determines the distribution of the swirl or rotation in the field. This coupling may lead to instabilities in the solution process.

2-3-3. THE TURBULENT MODEL: Spalart-Allmaras Model

The Spalart and Allmaras turbulence model has been implemented in a finite volume code using an implicit finite difference technique. A wide range of turbulent flows have been computed to validate the implementation and numerical results are shown. The Spalart-Allmaras model belongs to the family of eddy viscosity models. This family of the models is based on the assumption that

the Reynolds stress tensor $(-\rho u_i u_j)$ is related to the mean strain rate through an apparent turbulent viscosity called eddy viscosity ν_T

$$-\overline{u_i u_j} = v_T \left(\frac{\partial \overline{u_i}}{\partial y_j} + \frac{\partial \overline{u_j}}{\partial y_i} \right)$$

In the Spalart-Allmaras model, the eddy viscosity is computed through a partial differential equation. In particular the eddy viscosity ν_T computed by an intermediate variable $\widetilde{\nu}$ through the relation

$$v_T = \widetilde{v} f_{v1}(\chi)$$

Where χ is the ratio

$$\chi = \frac{\widetilde{v}}{v}$$

And f_{v1} is a damping function. The intermediate variable \widetilde{v} is computed by solving a differential equation that can be written in compact form as

$$\frac{D\widetilde{v}}{Dt} = b_{prod}(S, \widetilde{v}, d) - b_{dest}(\widetilde{v}, d) + b_{trip}(d_T) + \frac{1}{\sigma} \left[\nabla ((v + \widetilde{v})\nabla \widetilde{v}) + c_{b2}(\nabla \widetilde{v})^2 \right]$$

Where the symbols b_{prod} and b_{dest} indicate respectively the production term and the destruction term and finally b_{trip} denotes a special source term which allows the laminar-turbulent transition in a fixed point. It should be pointed out that, although the transition on set point has to be user-specified; the flow development in the transition region is built into the model through the trip source term, b_{trip} . The

quantities enclosed between the brackets show the main depending variables of these source terms. In particular S means the vorticity magnitude. d is the wall distance and d_T is the distance from the transition point. the last term is a diffusion term in which σ and c_{b2} indicate respectively the turbulent Prandtl Number and a calibration constant.

CHAPTER 3

RESULTS AND DISCUSSIONS

3-1. COMPARATIVE ANALYSIS

This section presents qualitative and quantitative descriptions of the flow in the vaneless diffuser of the centrifugal compressor. All of the experimental data was supplied by Turbomachinary Laboratory Michigan State University. And the experimental results and the computational results were compared in this section clearly.

Figure 4 through 7 show both the computational and experimental results of the cases of the four different rotational speeds at the each sections, 13000, 15500, 18000, and 20500 (rpm) and λ =1.06, 1.15, 1.23, 1.38, 1.60, 1.83, and 1.93 of ...

- ➤ Absolute radial and swirl velocities: Cr/U₂, Cu/U₂
- \triangleright Total pressure and Total temperature: π , τ
- \triangleright Flow Angle: α (°)

"*" and "e" indicate the computational and the experimental data respectively. "z/b" means "height/ inlet height", the distance toward the hub from the shroud at the diffuser inlet. And " λ " is "diameter/ inlet diameter" the distance of the flow direction from inlet to exit.

3-1-1. FLOW VELOCITIES AND THERMODYNAMIC PROPERTIES

According to all of figures (Figure 4 to 7), they show that the computational results are quite similar to the experimental results.

On the Figure 4-1, the radial and swirl velocities are shown as different from each other at the inlet. But at the outlet, the velocities become almost same values.

Figure 4-2 shows that the distributions of total pressure are always flat thought inlet to outlet. And Figure 4-3 shows that there is a difference between the computational and experimental results of flow angle, where z/b is around 0.7 to 1.0. Furthermore the difference becomes bigger around middle section (λ =1.23 – 1.6). After that, the difference disappears and experimental and computational results indicate alike values.

The radial velocity of C.F.D results shows lower than the experimental data and the radial velocity make the flow angle of C.F.D results smaller then experimental (Figure 4-1 and 4-3). As well as Figure 4-1, Figure 5-1 also shows smaller radial velocities at the same positions where $\lambda = 1.23$ to 1.6 and z/b=0.7 to 1.0. It is conceivable that the inlet velocity conditions affect this phenomenon. Because there is a huge reverse flow region at inlet-shroud corner, that causes counterclockwise rotation in entire flow field. The counterclockwise rotation leads the radial velocity of hub side smaller and makes the gap between experimental and computational results. In addition, the inlet reverse flow region becomes larger as well as the rotational speed becomes bigger. This makes rather stronger counterclockwise rotation of entire flow field. Thereby, the radial velocities of hub side at the higher rotational speed become smaller.

On the other hand, the distributions of total pressure and total temperature show nice results which are those nice flat distributions of total pressure and constant and uniform temperature (Figure 5-2).

Figure 5-3 shows good results such as the reverse flow at the corner of inlet and hub and almost uniform flow with 45 degree flow angle around the exit.

3-1-2. CONTOURS

This section presents the contours of flow angle α , absolute radial velocity Cr/U_2 , total pressure π , absolute swirl velocity Cu/U_2 , velocity magnitude, velocity vectors, and total temperature τ (Figure 8 through 11). Absolute radial and swirl velocities are normalized by impeller rotational speed, U_2 .

According to the figures of the absolute radial velocities, the flow tends to lean to the shroud side when the rotational speed becomes higher. The reason is that the reverse flow region at the corner of inlet and shroud side is getting bigger when the rotational speed becomes higher, and this causes to appear the big stagnation region at the corner. In the same way, the figures of the flow angle and the total pressure show the similar phenomenon.

Figure 8-4 (B) shows that the distribution of swirl velocity at low rotational speed indicates horizontal. But when the rotational speed becomes higher, the distribution becomes tilted shape (Figure 11-4 (B)). Initial inlet boundary condones can explain this phenomenon. Figure 3 shows that the swirl velocity of hub side (z/b=1.0) is always higher than shroud side (z/b=0).

3-2. PREDICTIVE ANALYSIS

Figure 12 shows the fifteen cases of inlet conditions of each rotational speed which were predicted from the four experimental data: 13000, 15500, 18000, and 20500 rpm. Those inlet boundary conditions of 0 to 13000 rpm and 20500 to 33000 rpm were predicted from four conditions of the experimental data. All of these data were computed and flow angle α , total pressure π , radial velocity Cr, swirl velocity Cu, velocity magnitude, and path line were created and discussed through those rotational speeds (Figure 13 through 18).

Figure 13 shows that the distributions of flow angle are different along the passage, but rotational speed is getting higher, the distributions are getting same kind and the differences toward to hub-shroud are appearing clearly. Wide reverse flow region appears at the corner of inlet and shroud on 33,000 rpm

When rotational speed is around 18000 and 23,000 rpm, the flow tends to go to shroud side. But the rotational speed becomes higher, the flow becomes uniform again (Figure 14 and 15).

Figure 16 shows that horizontal distribution at the lower rotational speed and the distribution of tilted shape at the higher rotational speed. Furthermore, the highest swirl speed region tends to gather at the corner of inlet ant hub, when

rotational speed becomes higher.

Figures of velocity magnitude show an undiversified phenomenon through all of rotational speeds (Figure 17).

There is a huge vortex region at the inlet-shroud corner. And it continues till almost middle of passage at the shroud side (Figure 18).

CHAPTER 4

CONCLUSIONS AND FUTURE WORK

4. CONCLUSIONS AND FUTURE WORK

This paper has presented the results obtained, using computational simulations, on a vaneless diffuser with the experimental results. The following conclusions were made:

- > The steady phenomena in the vaneless diffuser has been prospected
- ➤ The experimental and computational data have been compared clearly
- > The effect of input conditions has been investigated

As a future work, three-dimensional simulations are recommended. The effect of the input conditions was very obvious. But the differences between CFD and Experimental results of radial and swirl velocities around $\lambda = 1.23$ were not analyzed clearly. It is estimated that tangential (axial) velocity component might

be related to this problem. Therefore, in order to explain about the movement of axial velocity and more detail of inlet boundary conditions, three-dimensional simulation is necessary.

•

BIBLIOGRAPHY

LIST OF BIBLIOGRAPHY

Rautenberg, M. (1976). <u>Experimental and Theoretical Research of Flow Condition of Diffuser of High Flow Rate Centrifugal Compressor</u>. Institute of Jet Engine, University of Hannover, Germany

Turunen-Saaresti, T. (2004). <u>Computational and Experimental Analysis of Flow Field in the Diffusers of Centrifugal Compressors</u>. Lappeenranta University of Technology

Phillips, D.G., Richards, P.J., Flay, R.G.J. <u>Diffuser Development for a Diffuser Augmented Wind Turbine Using Computational Fluid Dynamics</u>. Department of Mechanical Engineering, University of Auckland, New Zealand

Liu, R., Xu, Z. (2004). <u>Numerical Investigation of a High-Speed Centrifugal Compressor with Hub Vane Diffusers</u>. Institute of Fluid Machinery, School of Energy and Power Engineering, Xi'an Jiaotong University, China

Chapman, K. Jariwala, J. and Keshavarz, A. <u>Numerical Investigation of a Turbocharger Compressor with Variable Diffuser Vane Setting Angle</u>. National Gas Machinery Laboratory, Kansas State University

Hayashi, N, Koyama, M. and Ariga, I. <u>Study of Flow Patterns in Vaneless Diffusers of Centrifugal Compressors Using PIV</u>. Mechanical Engineering Department, Chiba Institute of Technology, Japan

Japikse, D. and Baines, N.C. (1998). <u>Diffuser Design Technology</u>. Concepts ETI, INC.

Fradin, C. (1992). <u>Detailed Measurements of the Flow Field in Vaneless And Vaned Diffusers of Centrifugal Compressors</u>. ONERA, Direction de l'Energétique, 29 Avenue de la Division Leclerc, 92320 Châtillon, France

Niazi, S., Stein, A. and Sankar, L. N. <u>Development and Application of A CFD Solver to the Simulation of Centrifugal Compressors</u>. School of Aerospace Engineering, Georgia Institute of Technology, Atlanta

Paciorri, R. and Deconinck, H. et al (1997). <u>Validation of the Spalart-Allmaras</u> <u>Turbulence Model for Application in Hypersonic Flows</u>. von Karman Institute for Fluid Dynamics, Sint-Genesius-Rode, Belgium

Fluent Inc. (1998). Fluent 5 Tutorial Guide. Fluent Incorporated

Fluent Inc. (1999). Gambit Tutorial Guide. Fluent Incorporated

Figures

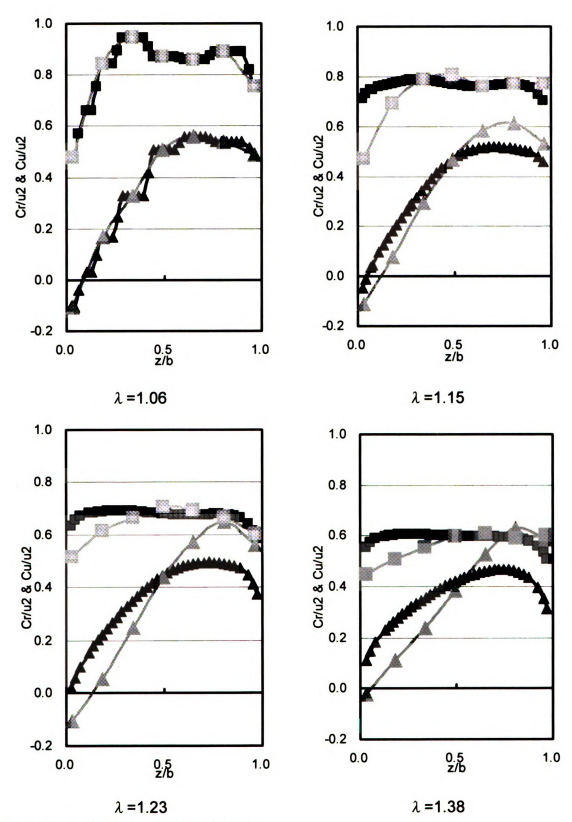


Figure 4-1: C.F.D vs. EXPERIMENT Absolute Radial and Swirl Velocity (Cr/U₂, Cu/U₂), n=13000 rpm

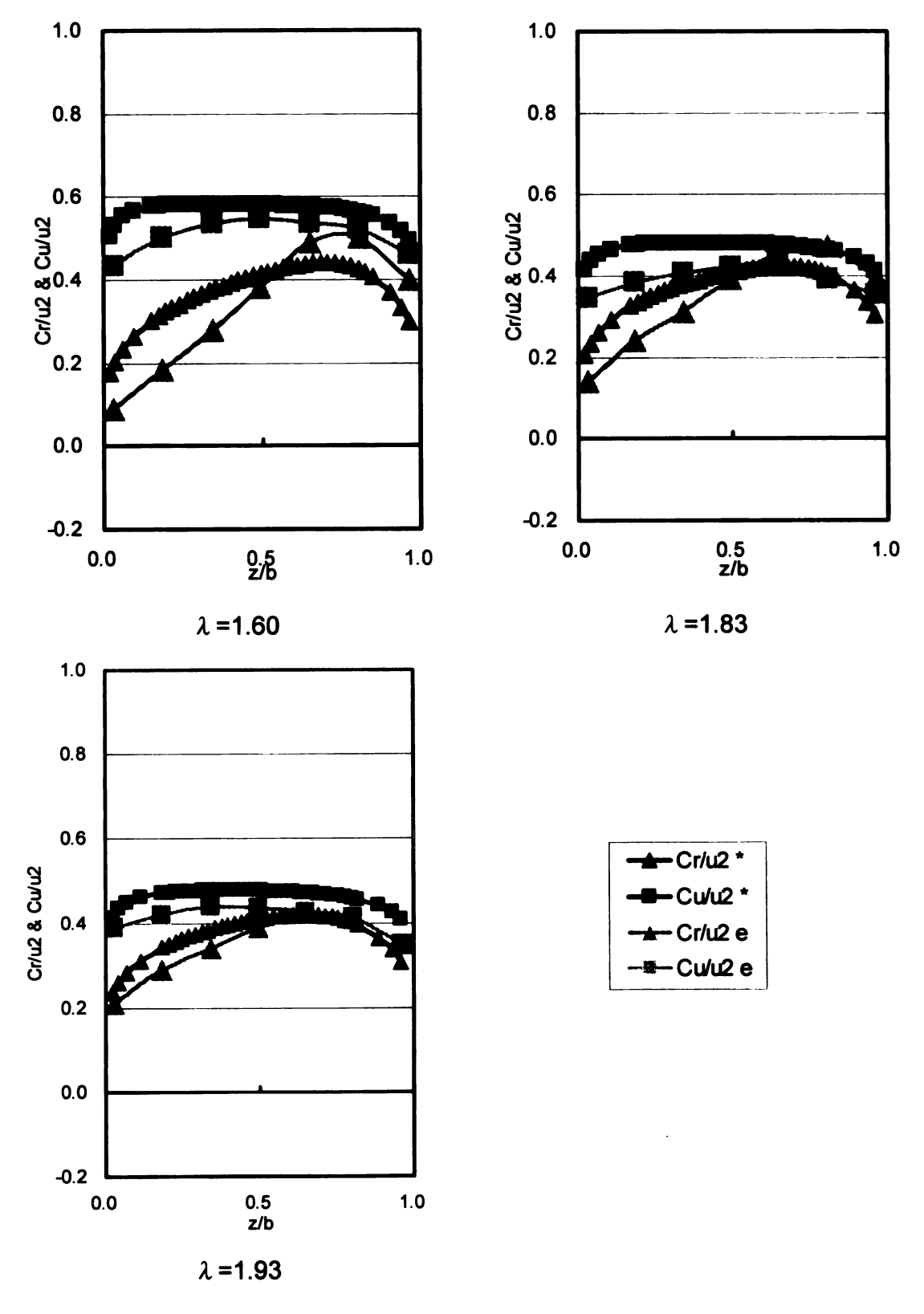


Figure 4-1 (cont'd)

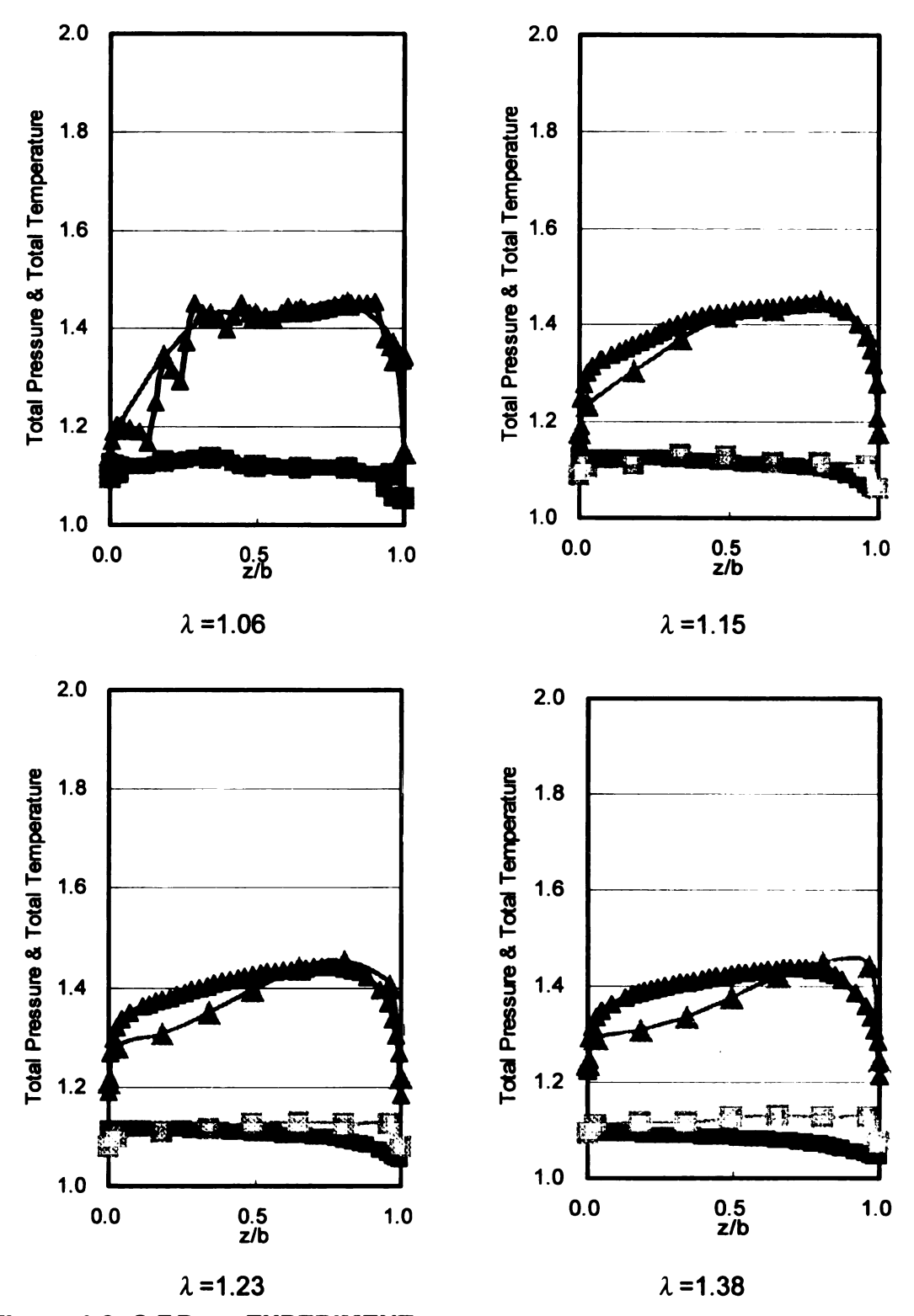


Figure 4-2: C.F.D vs. EXPERIMENT Total Pressure and Total Temperature ($\pi\,,~\tau$), n=13000 rpm

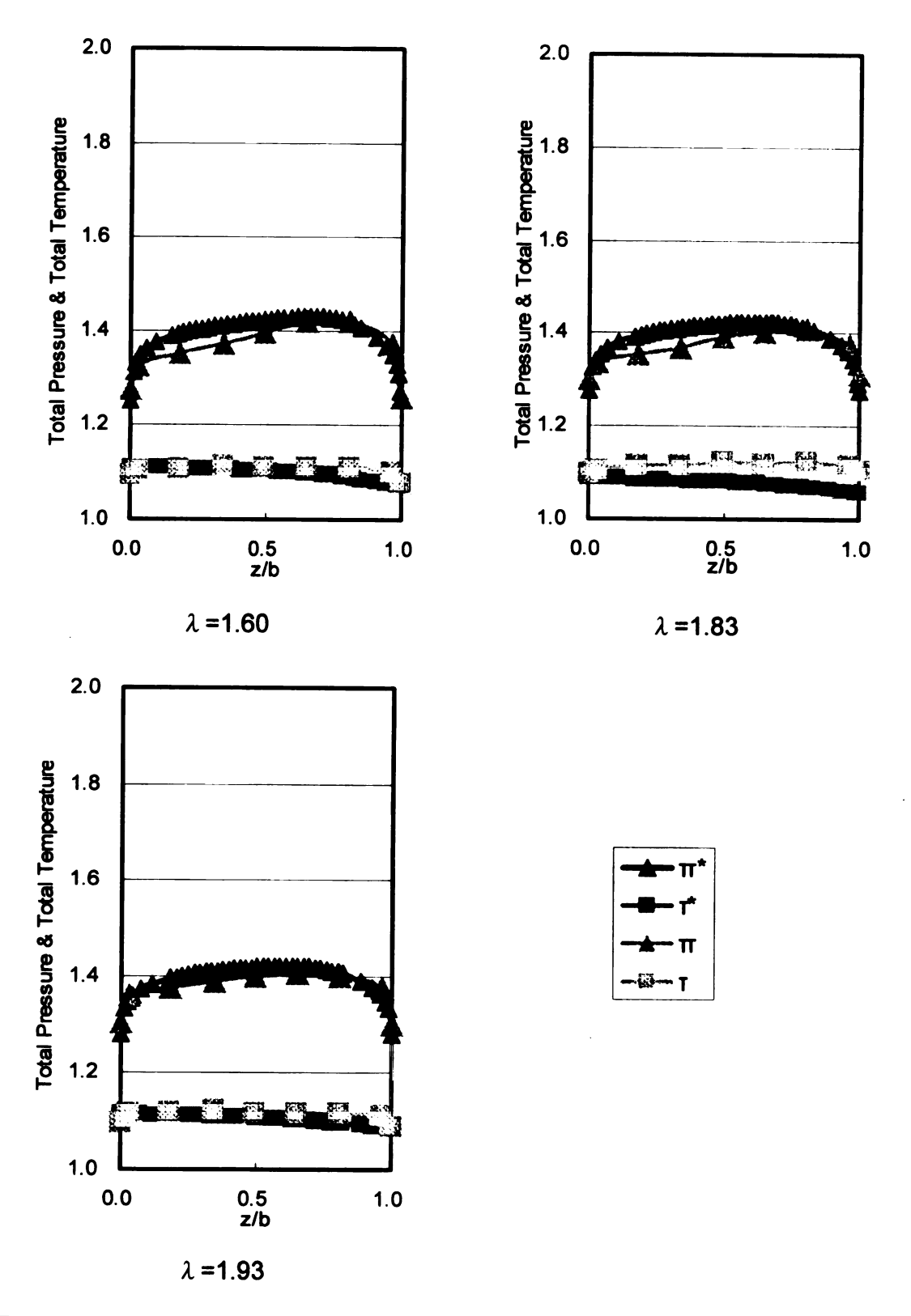


Figure 4-2 (cont'd)

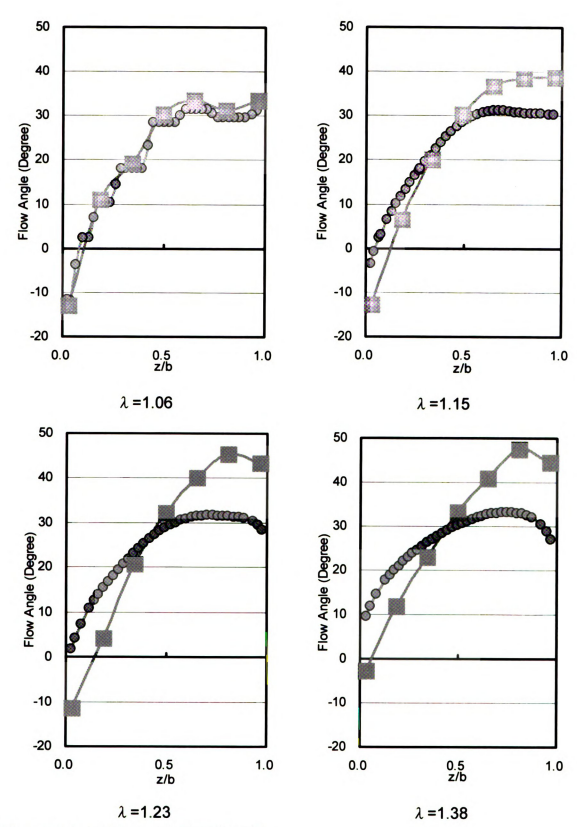


Figure 4-3: C.F.D vs. EXPERIMENT Flow Angle $\,\alpha$, n=13000 rpm

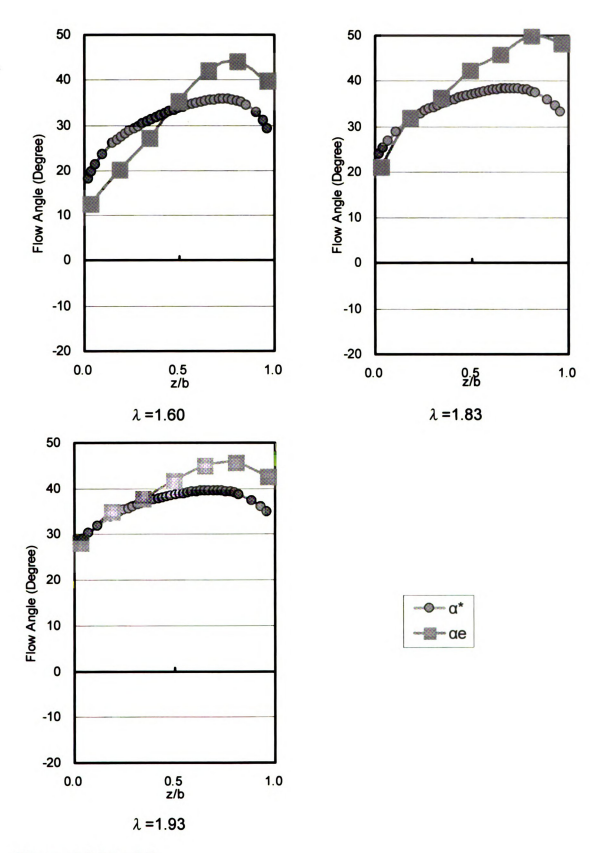


Figure 4-3 (cont'd)

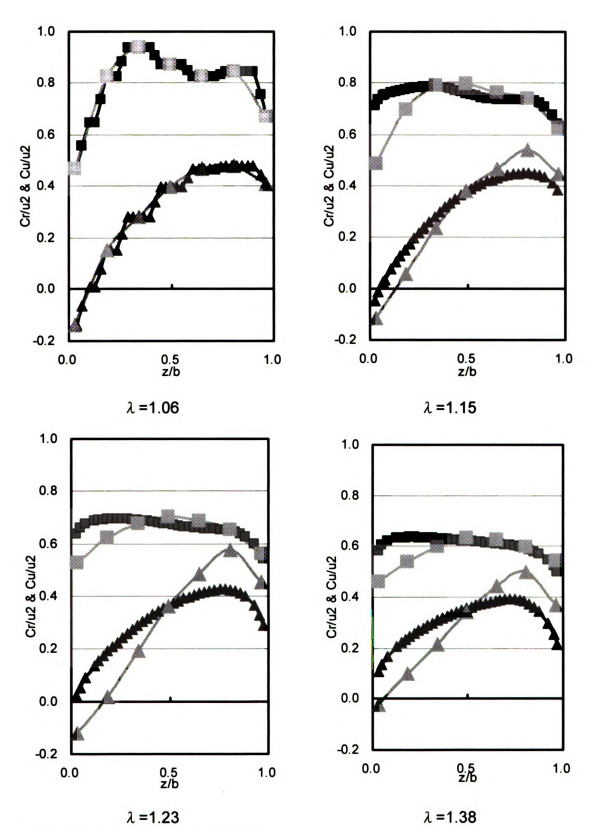


Figure 5-1: C.F.D vs. EXPERIMENT Absolute Radial and Swirl Velocity (Cr/U₂, Cu/U₂), n=15500 rpm

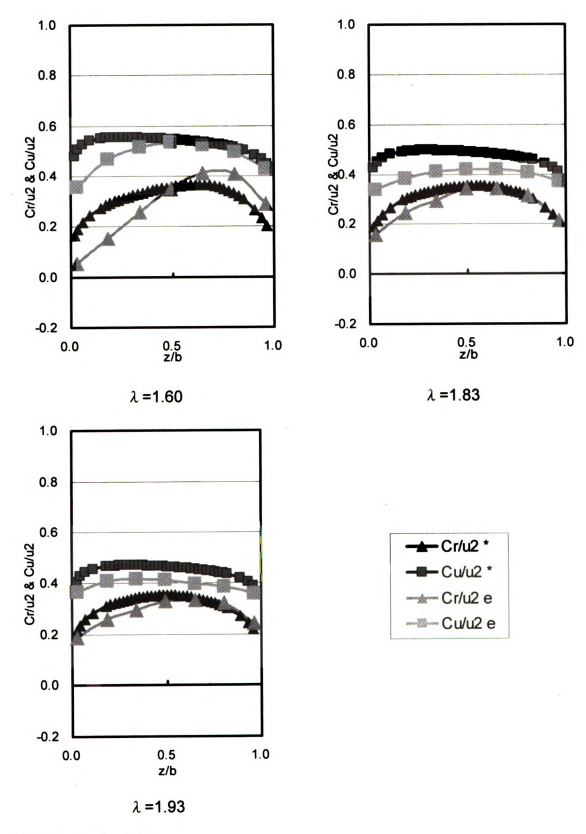


Figure 5-1 (cont'd)

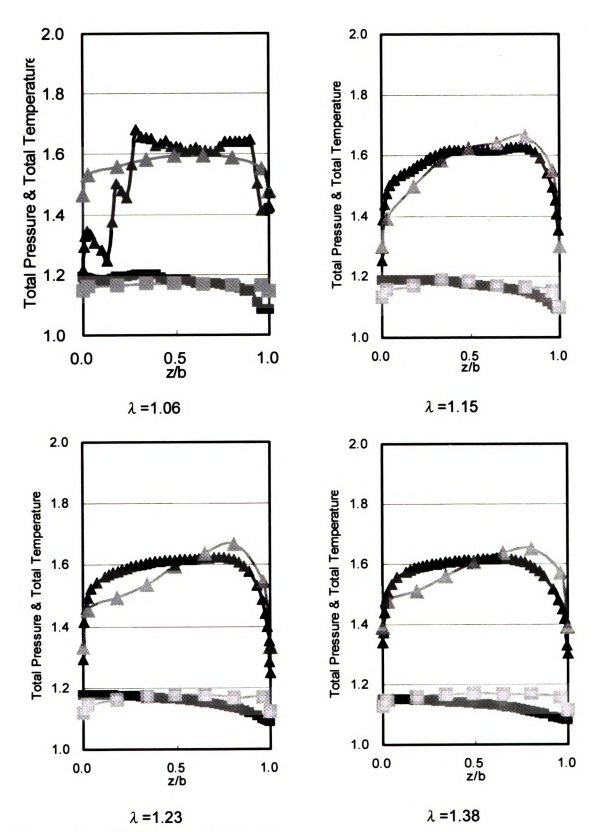


Figure 5-2: C.F.D vs. EXPERIMENT Total Pressure and Total Temperature (π , τ), n=15500 rpm

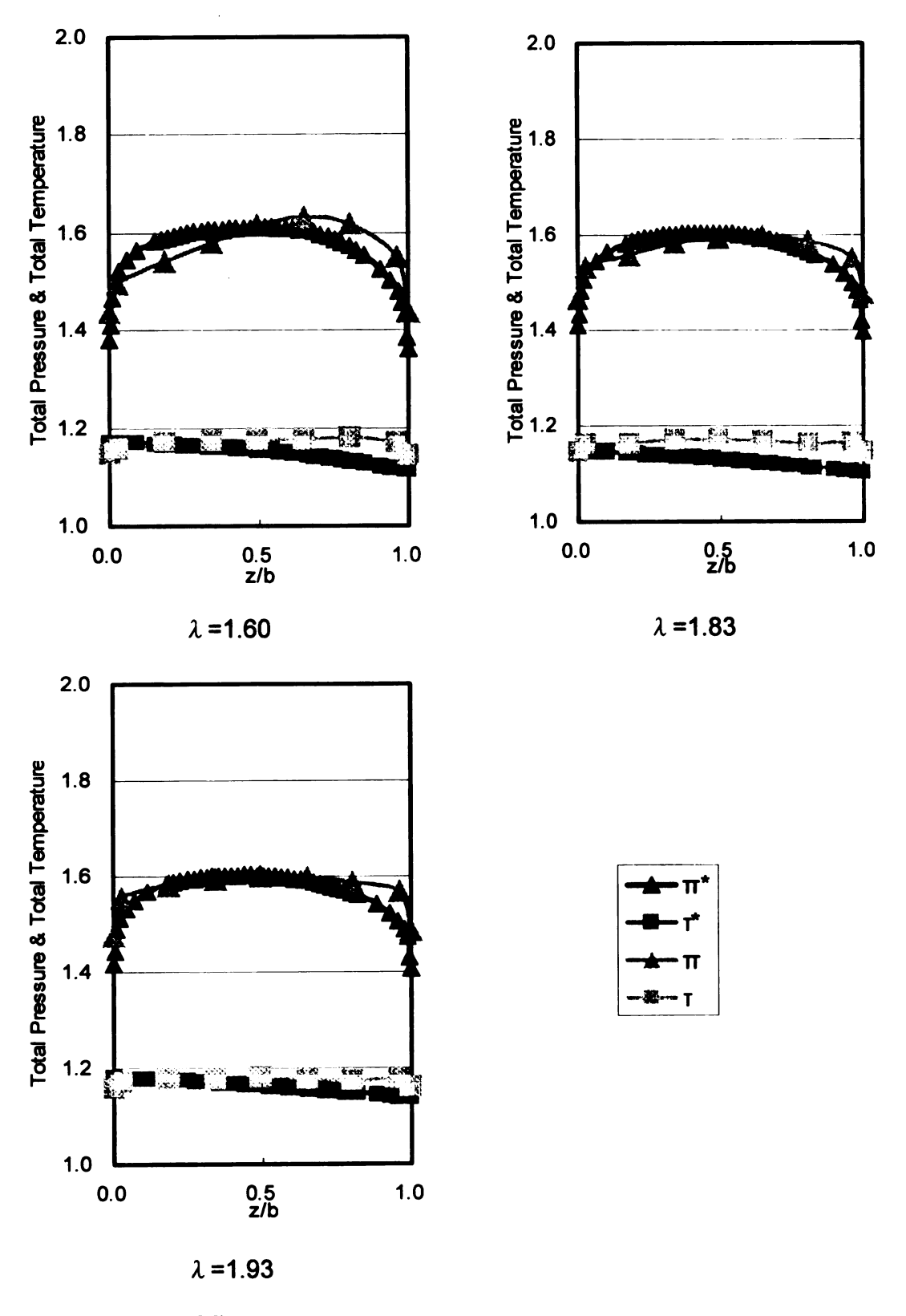


Figure 5-2 (cont'd)

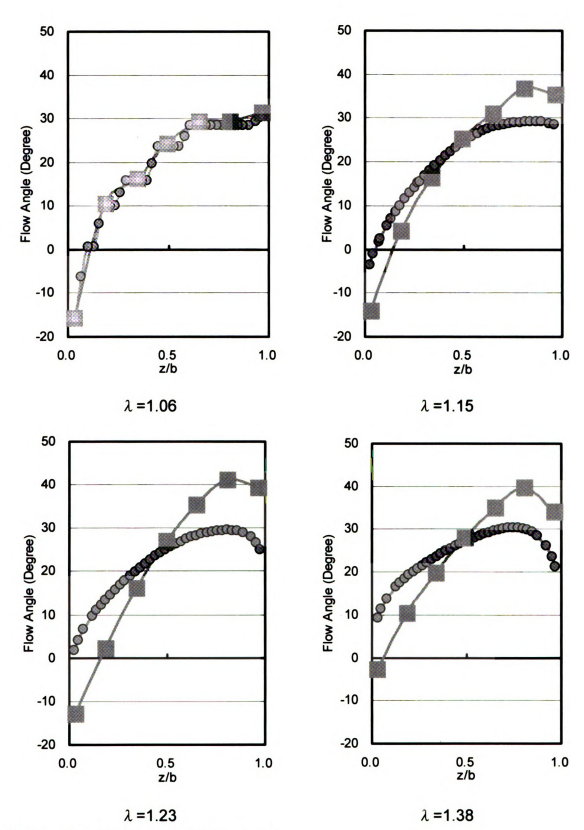


Figure 5-3: C.F.D vs. EXPERIMENT Flow Angle α , n=15500 rpm

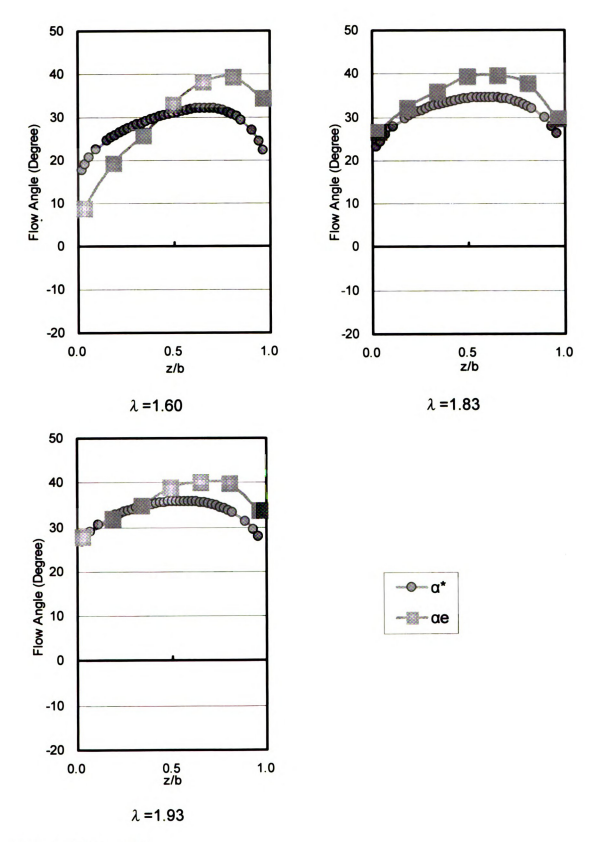


Figure 5-3 (cont'd)

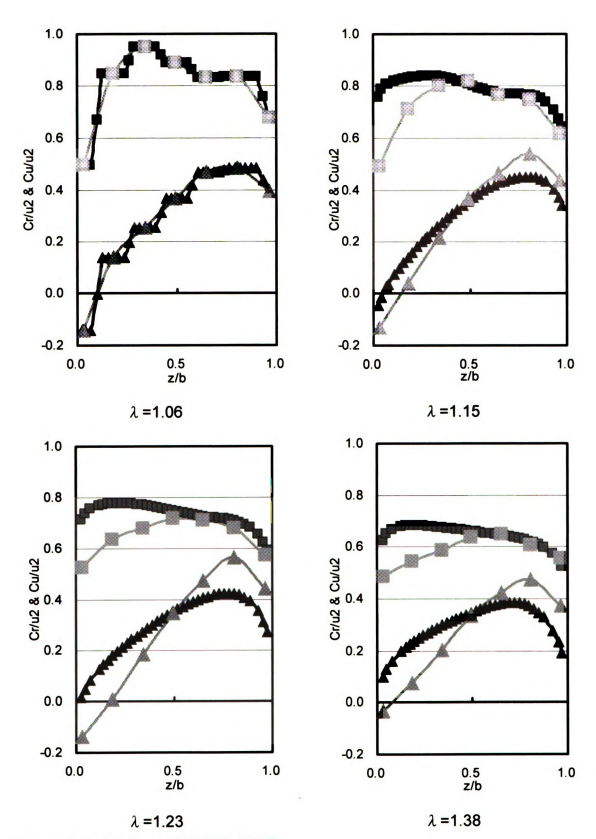


Figure 6-1: C.F.D vs. EXPERIMENT Absolute Radial and Swirl Velocity (Cr/U₂, Cu/U₂), n=18000 rpm

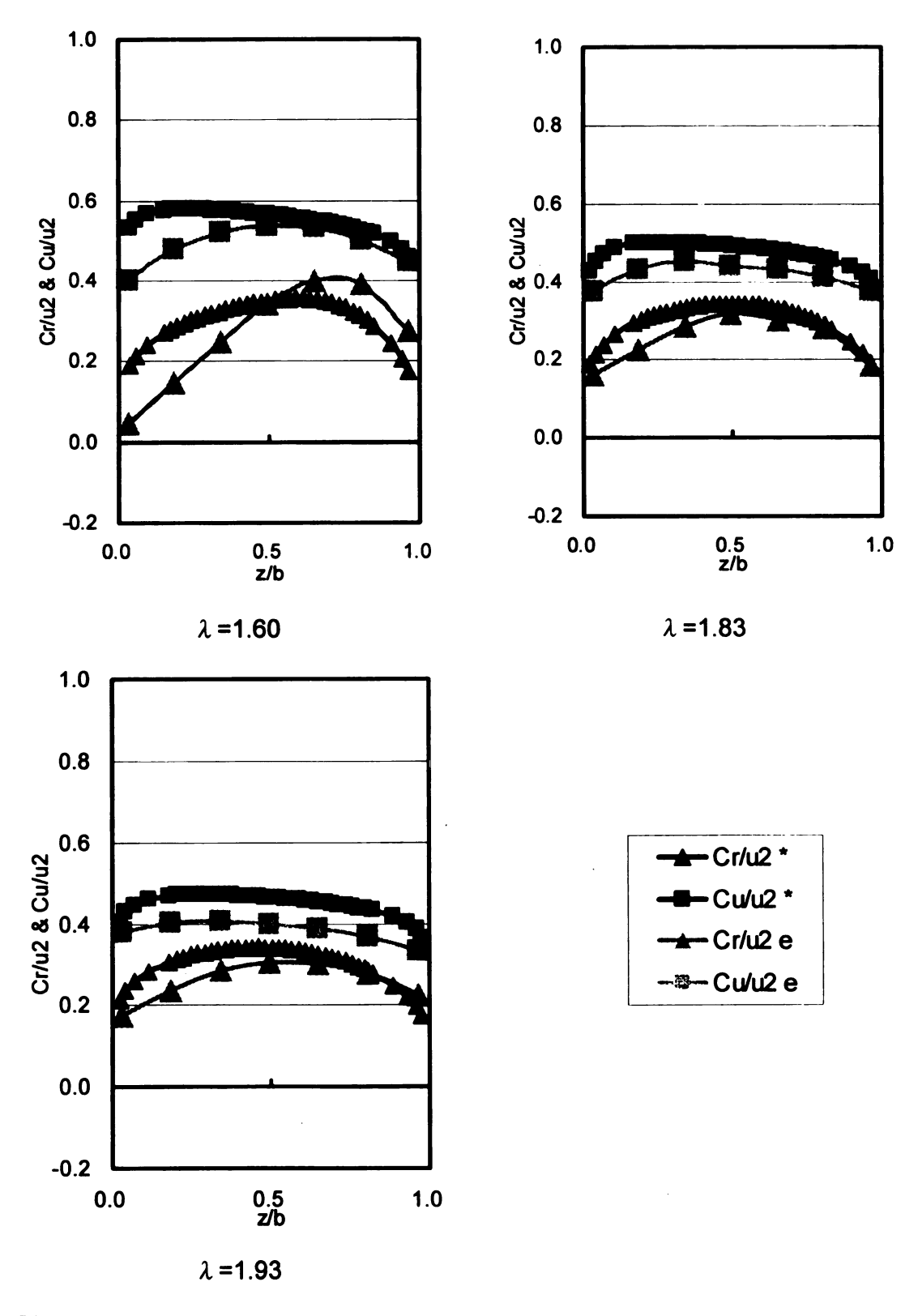


Figure 6-1 (cont'd)

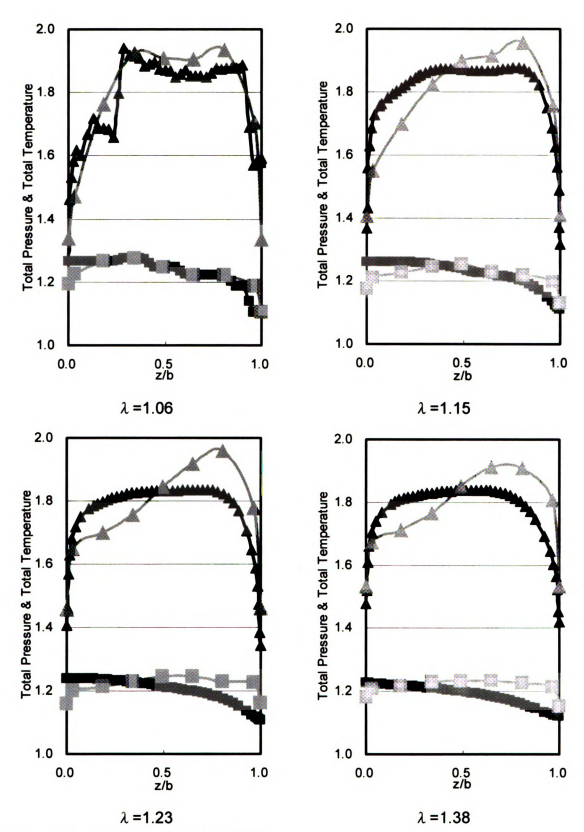


Figure 6-2: C.F.D vs. EXPERIMENT Total Pressure and Total Temperature (π , τ), n=18000 rpm

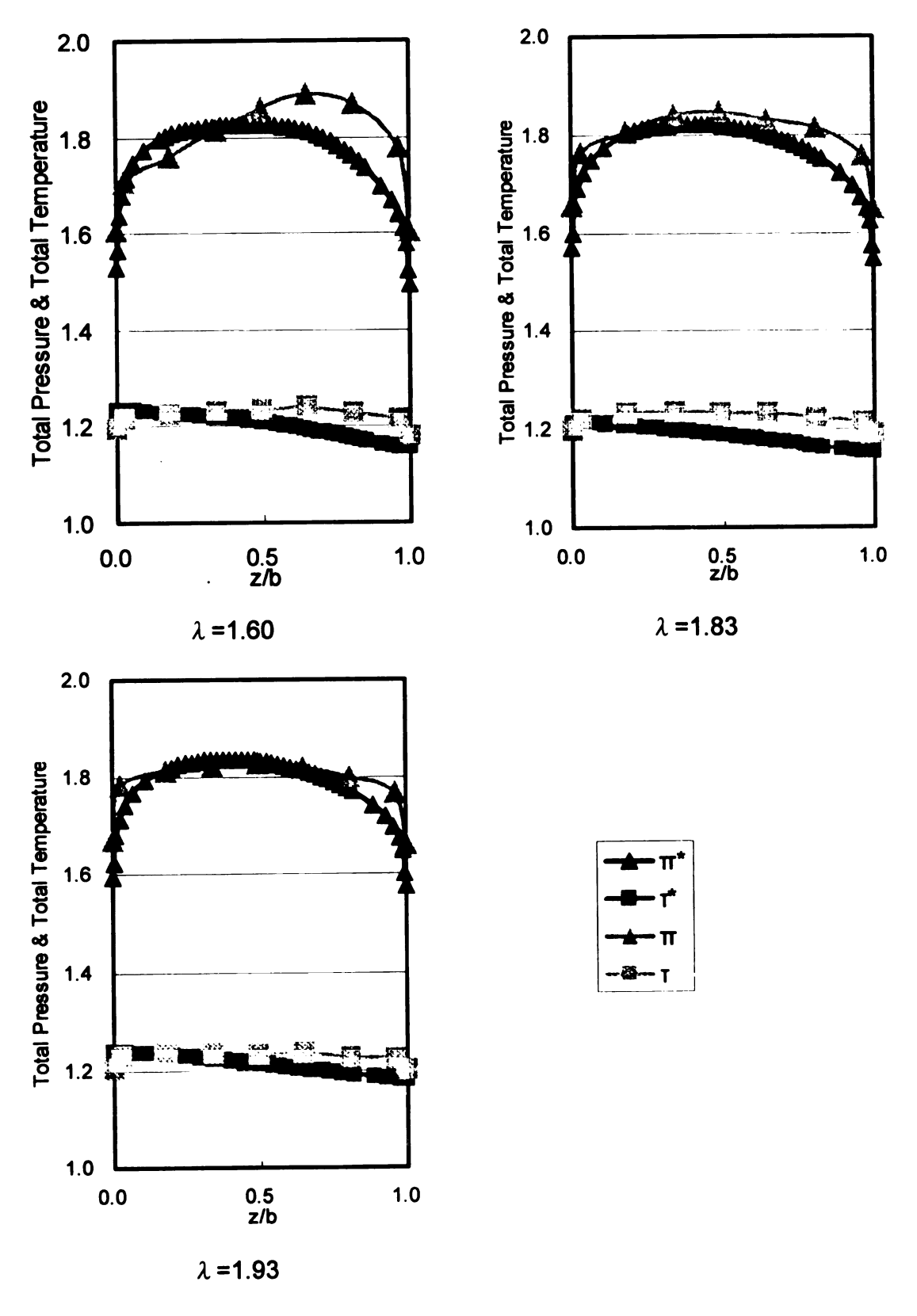


Figure 6-2 (cont'd)

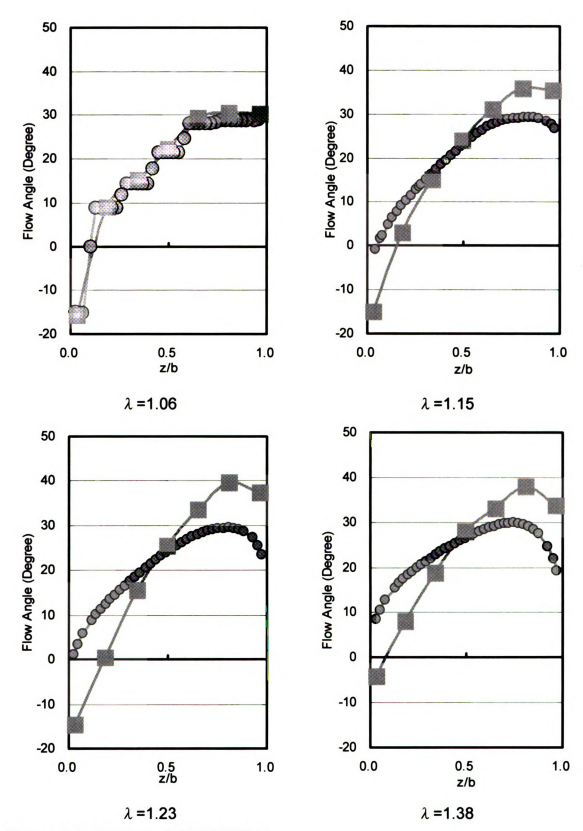


Figure 6-3: C.F.D vs. EXPERIMENT Flow Angle $\,\alpha$, n=18000 rpm

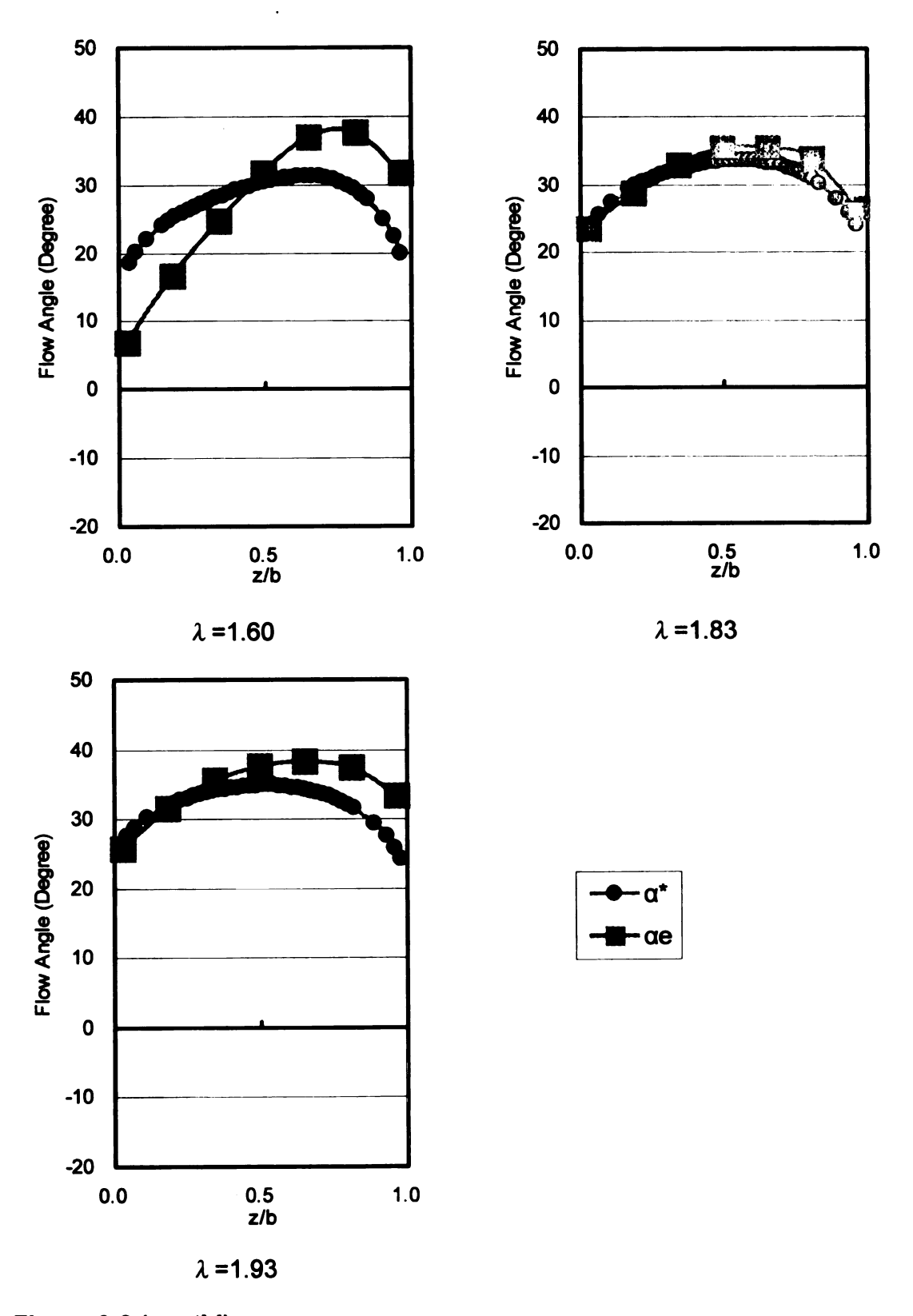


Figure 6-3 (cont'd)

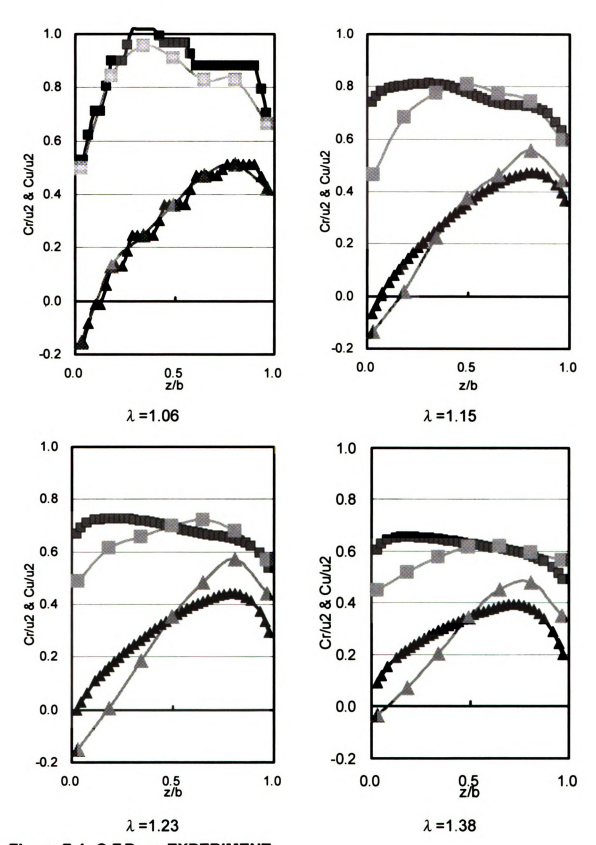


Figure 7-1: C.F.D vs. EXPERIMENT Absolute Radial and Swirl Velocity (Cr/U₂, Cu/U₂), n=20500 rpm

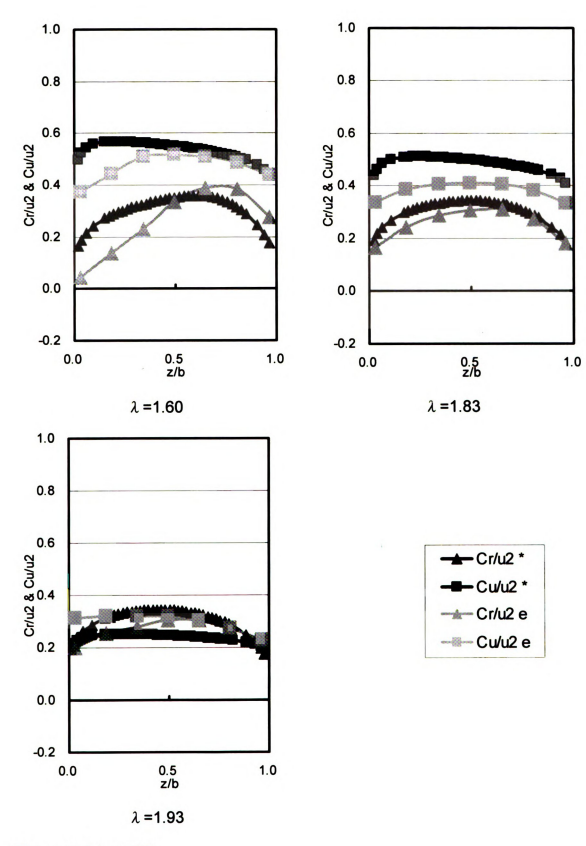


Figure 7-1 (cont'd)

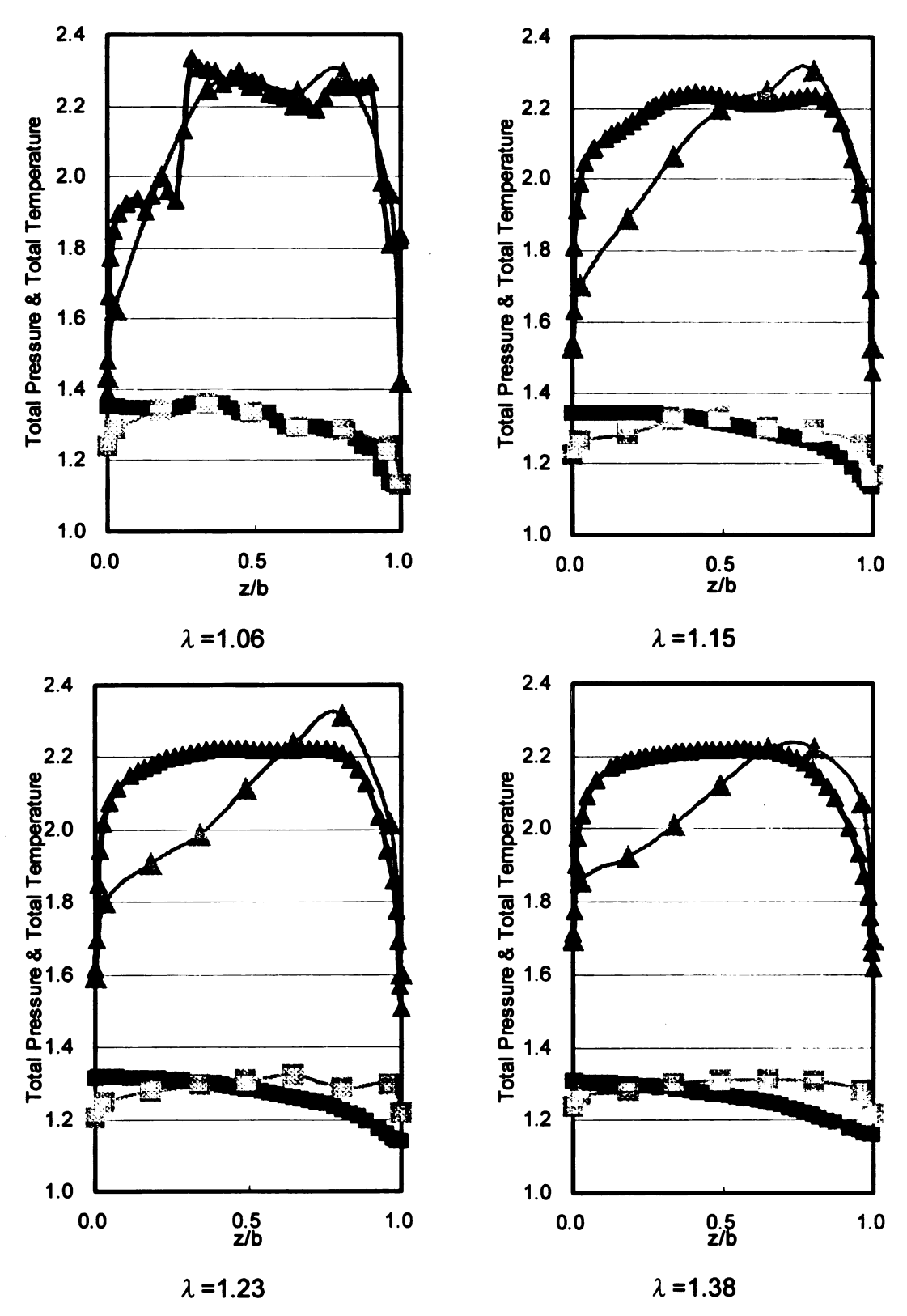


Figure 7-2: C.F.D vs. EXPERIMENT Total Pressure and Total Temperature (π , τ), n=20500 rpm

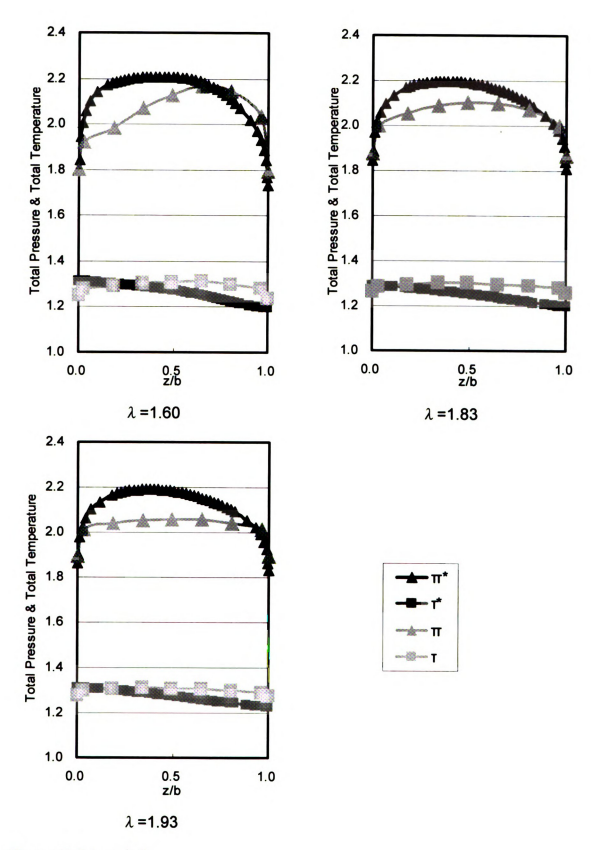


Figure 7-2 (cont'd)

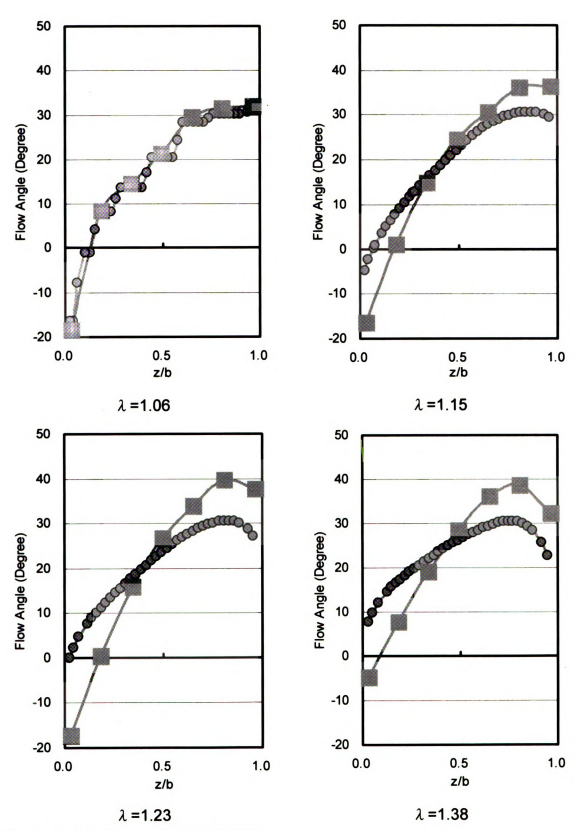


Figure 7-3: C.F.D vs. EXPERIMENT Flow Angle α , n=205000 rpm

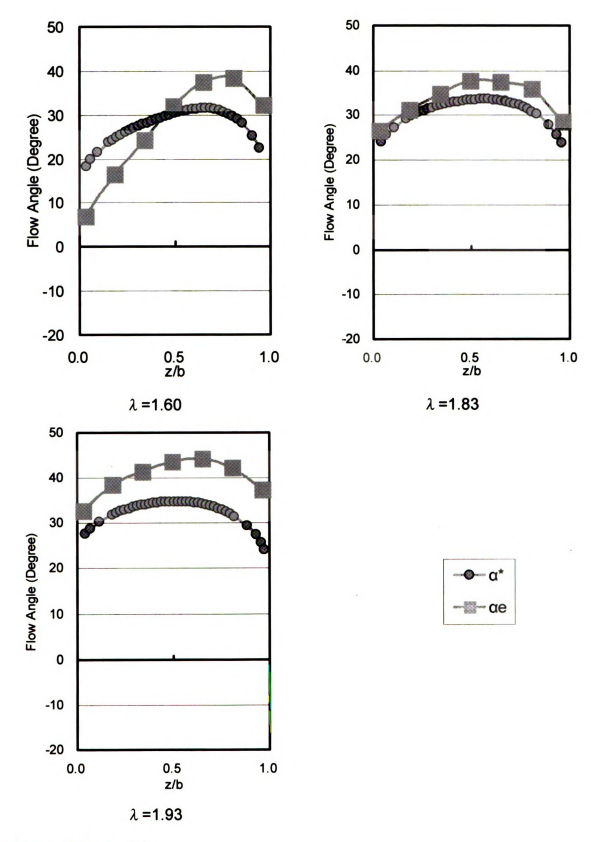
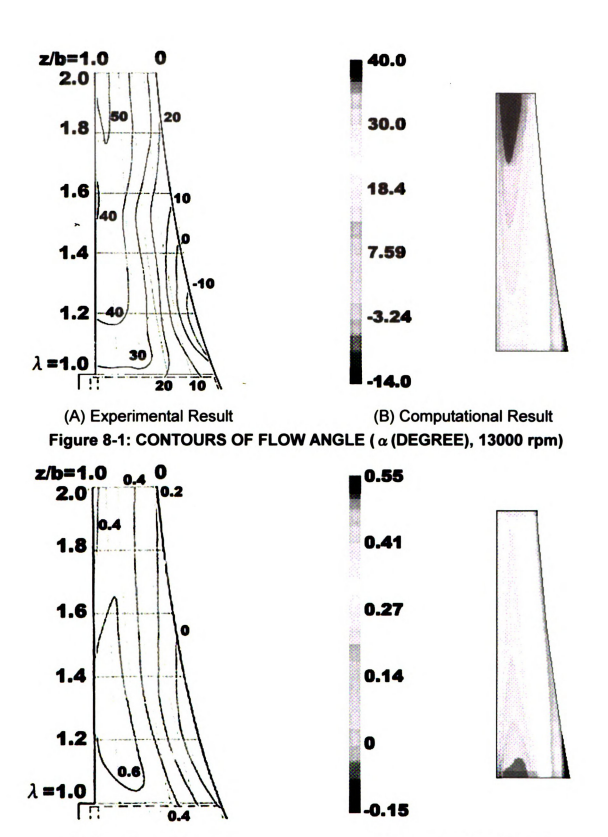


Figure 7-3 (cont'd)



(A) Experimental Result (B) Computational Result

Figure 8-2: CONTOURS OF ABSOLUTE RADIAL VELOCITY (Cr/U₂, 13000 rpm)

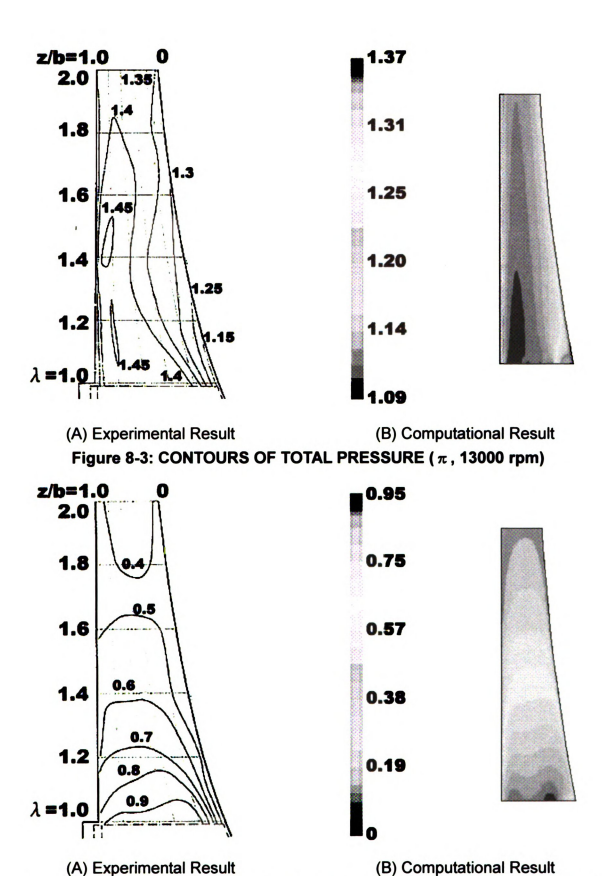


Figure 8-4: CONTOURS OF ABSOLUTE SWIRL VELOCITY (Cu/U₂, 13000 rpm)

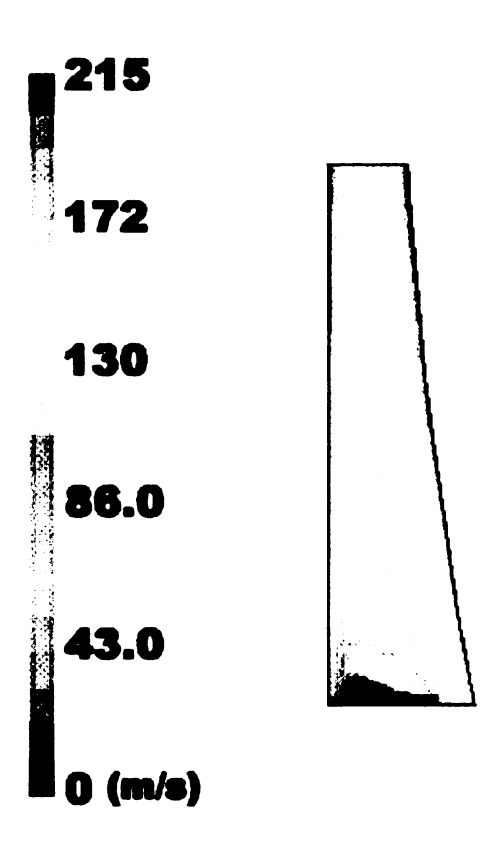


Figure 8-5: CONTOURS OF VELOCITY MAGNITUDE (m/s)

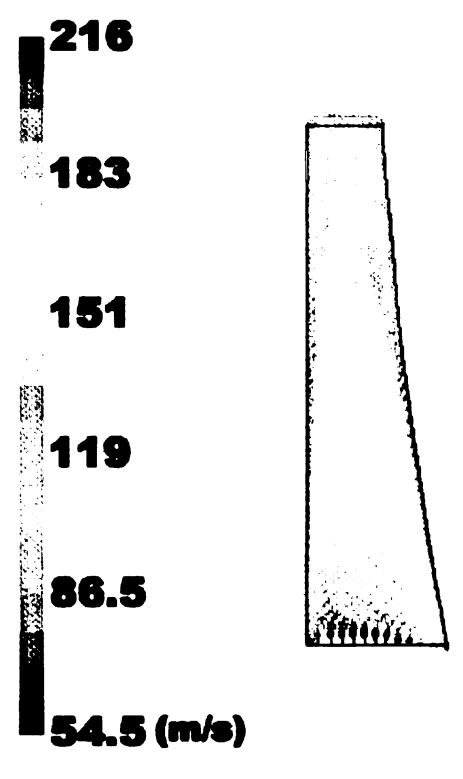


Figure 8-6: VELOCITY VECTORS COLORED BY VELOCITY MAGNITUDE n =13000 rpm

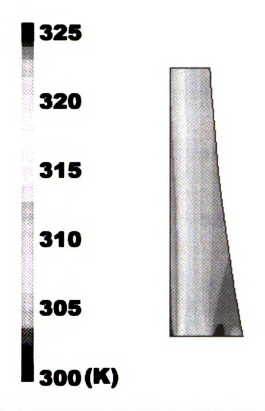
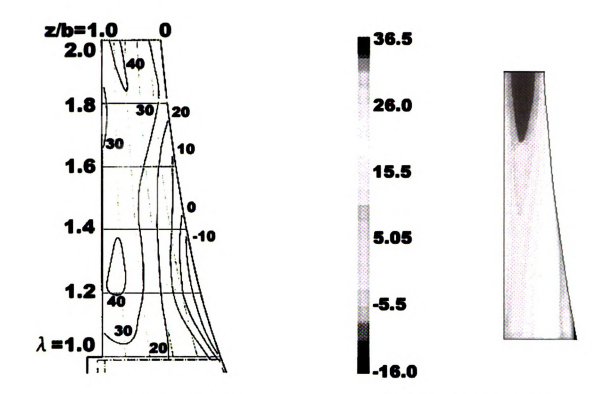
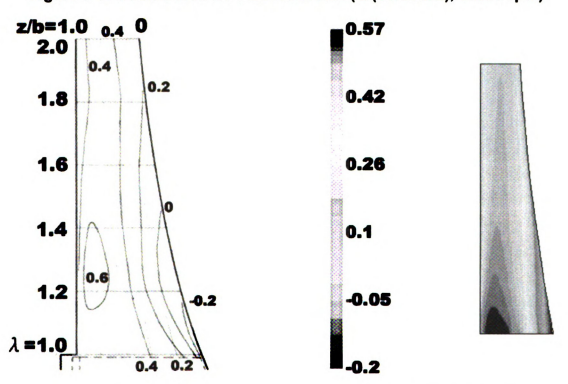


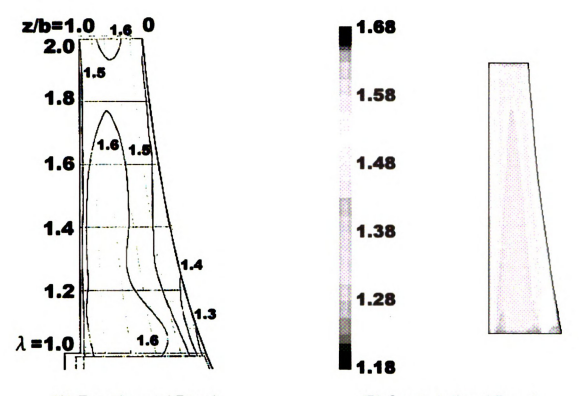
Figure 8-7: CONTOURS OF TOTAL TEMPERATURE (K)



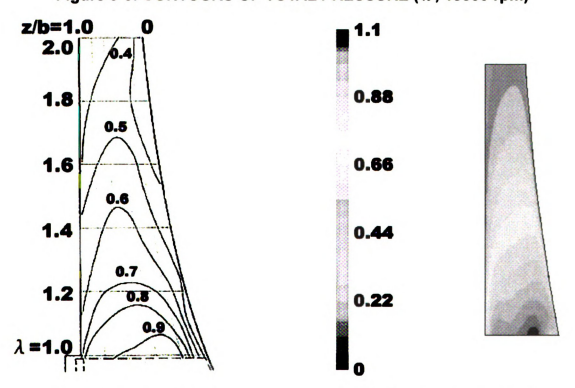
(A) Experimental Result (B) Computational Result Figure 9-1: CONTOURS OF FLOW ANGLE (\(\alpha\) (DEGREE), 15500 rpm)



(A) Experimental Result (B) Computational Result Figure 9-2: CONTOURS OF ABSOLUTE RADIAL VELOCITY (Cr/U₂, 15500 rpm)



(A) Experimental Result (B) Computational Result Figure 9-3: CONTOURS OF TOTAL PRESSURE (π , 15500 rpm)



(A) Experimental Result (B) Computational Result Figure 9-4: CONTOURS OF ABSOLUTE SWIRL VELOCITY (Cu/U₂, 15500 rpm)

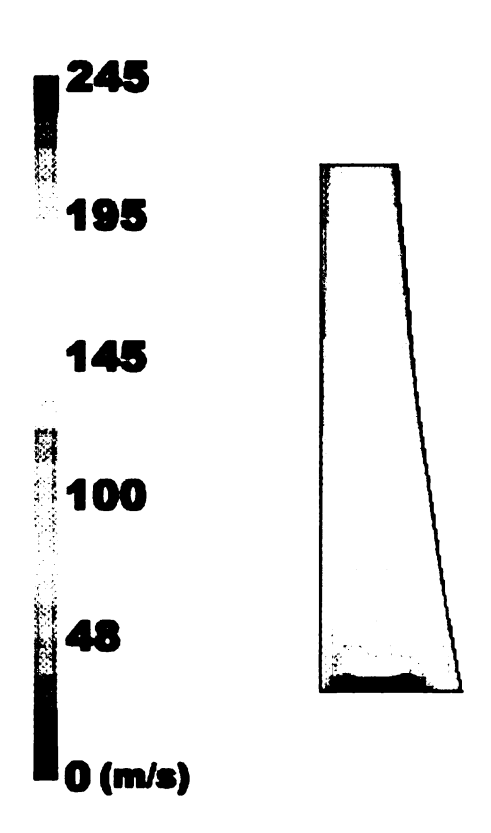


Figure 9-5: CONTOURS OF VELOCITY MAGNITUDE (m/s)

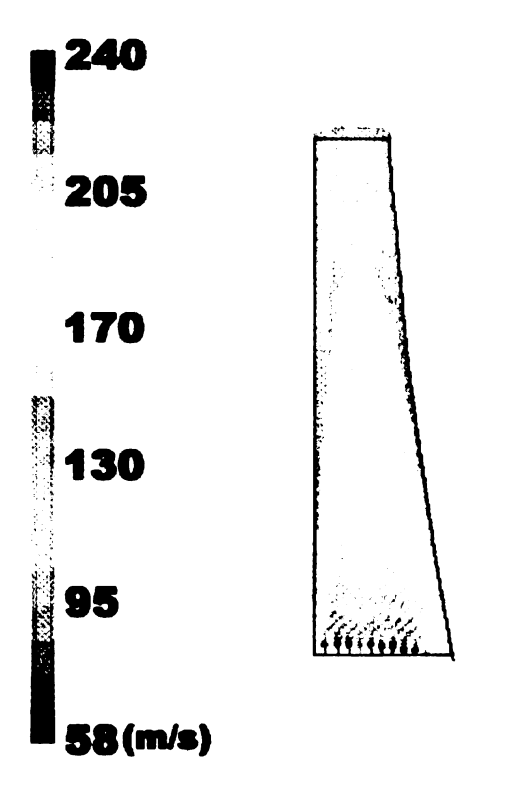


Figure 9-6: VELOCITY VECTORS COLORED BY VELOCITY MAGNITUDE n =15500 rpm

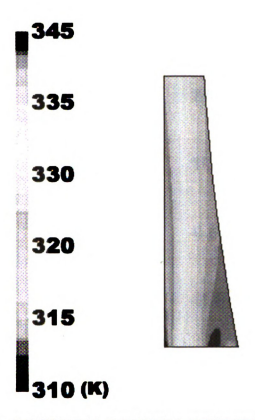
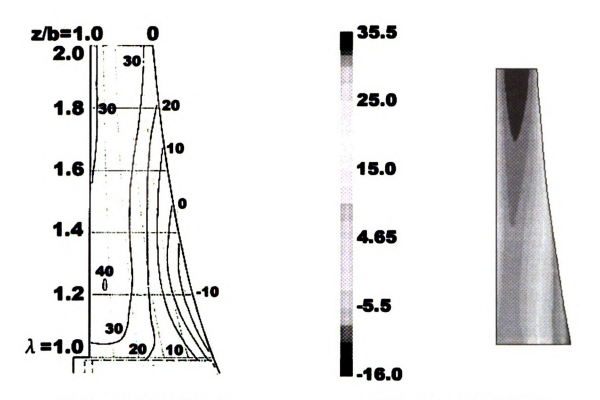
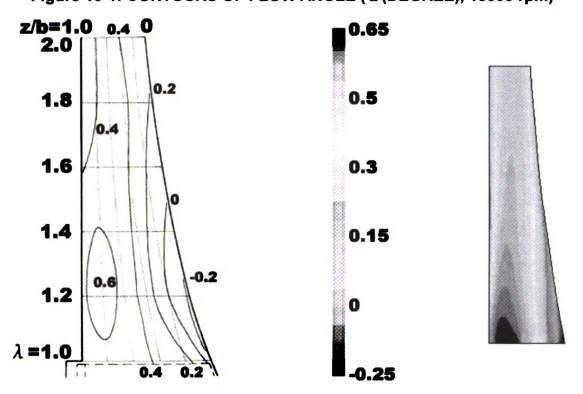


Figure 9-7: CONTOURS OF TOTAL TEMPERATURE (K)



(A) Experimental Result (B) Computational Result Figure 10-1: CONTOURS OF FLOW ANGLE (α (DEGREE), 18000 rpm)



(A) Experimental Result (B) Computational Result Figure 10-2: CONTOURS OF ABSOLUTE RADIAL VELOCITY (Cr/U₂, 18000 rpm)

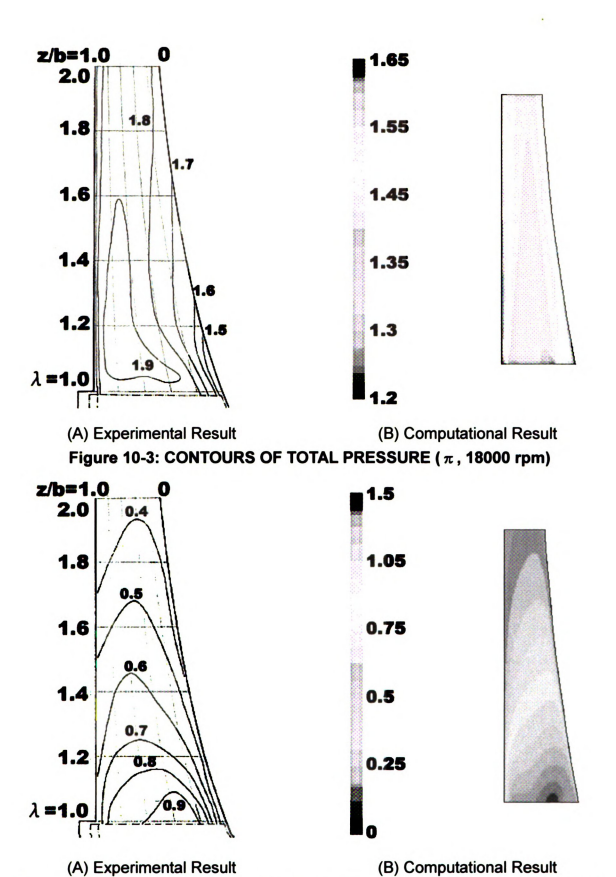


Figure 10-4: CONTOURS OF ABSOLUTE SWIRL VELOCITY (Cu/U₂, 18000 rpm)

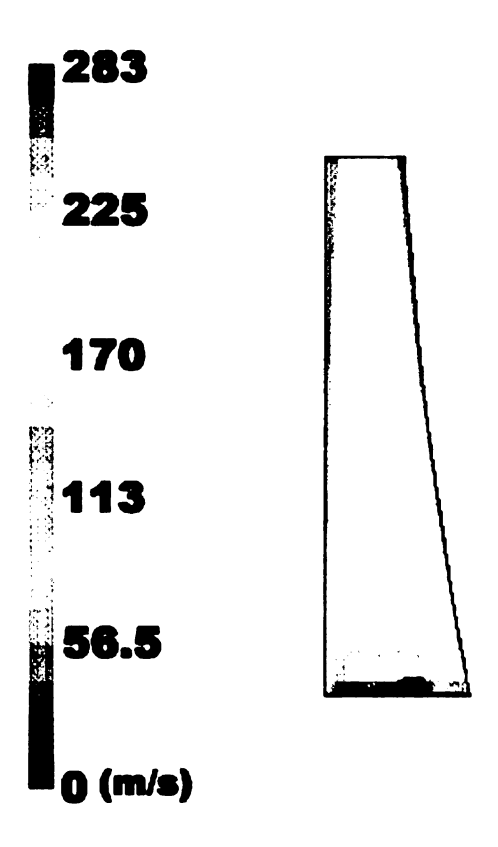


Figure 10-5: CONTOURS OF VELOCITY MAGNITUDE (m/s)

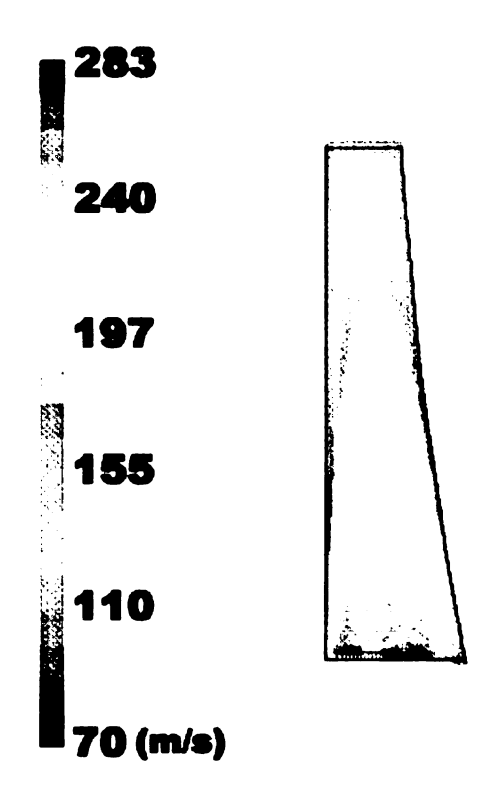


Figure 10-6: VELOCITY VECTORS COLORED BY VELOCITY MAGNITUDE n =18000 rpm

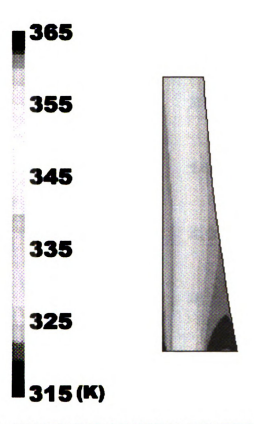
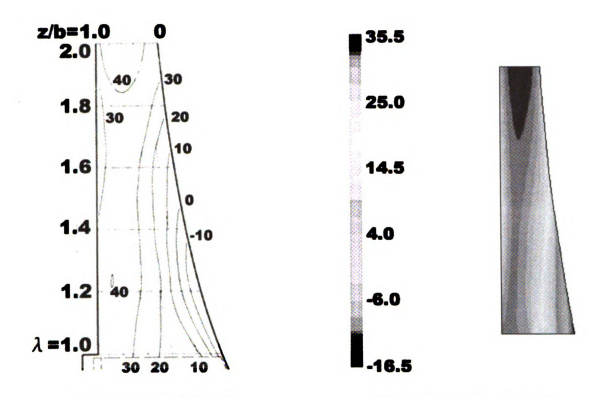


Figure 10-7: CONTOURS OF TOTAL TEMPERATURE (K)



(A) Experimental Result (B) Computational Result Figure 11-1: CONTOURS OF FLOW ANGLE (α (DEGREE), 20500 rpm)

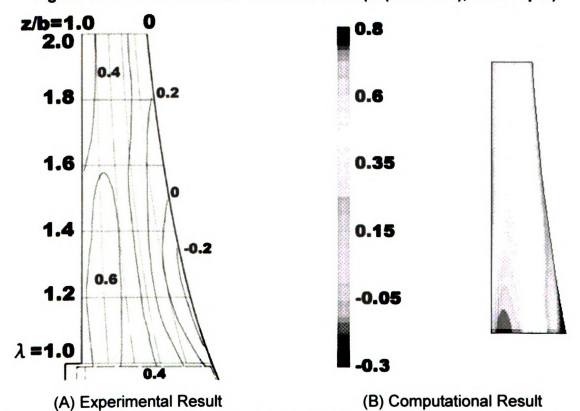
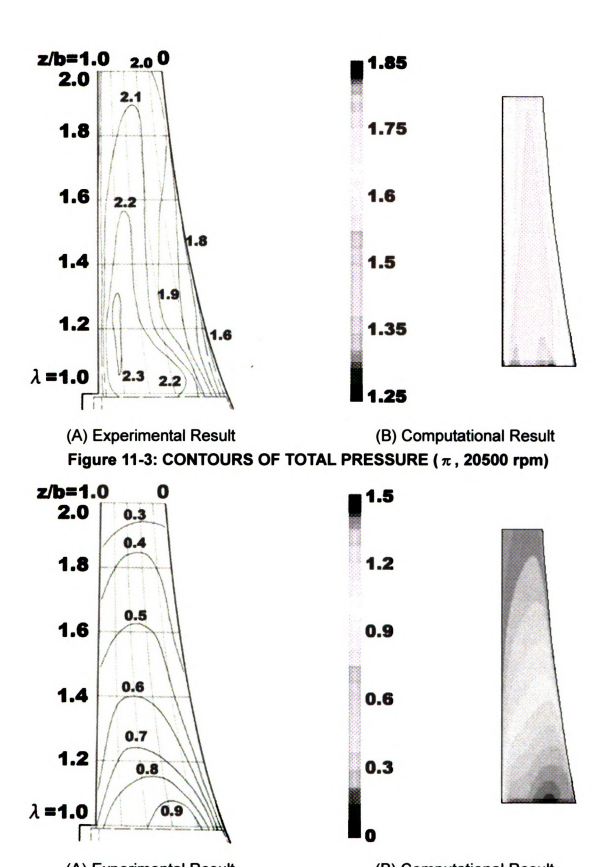


Figure 11-2: CONTOURS OF ABSOLUTE RADIAL VELOCITY (Cr/U₂, 20500 rpm)



(A) Experimental Result (B) Computational Result

Figure 11-4: CONTOURS OF ABSOLUTE SWIRL VELOCITY (Cu/U₂, 20500 rpm)

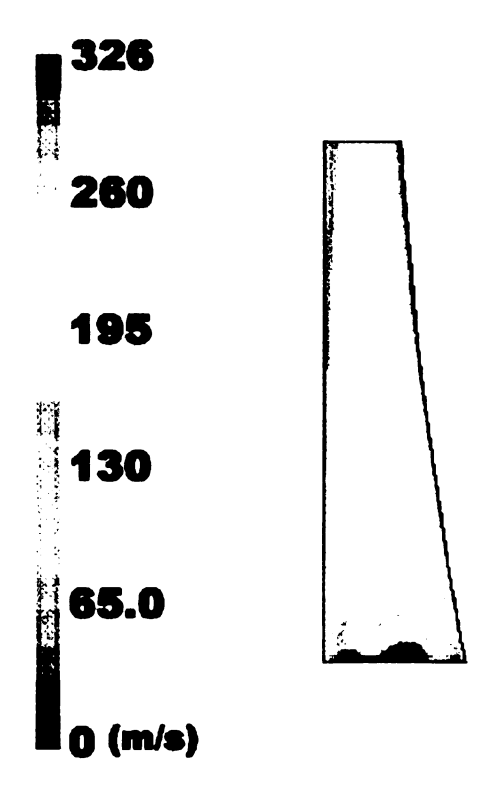


Figure 11-5: CONTOURS OF VELOCITY MAGNITUDE (m/s)

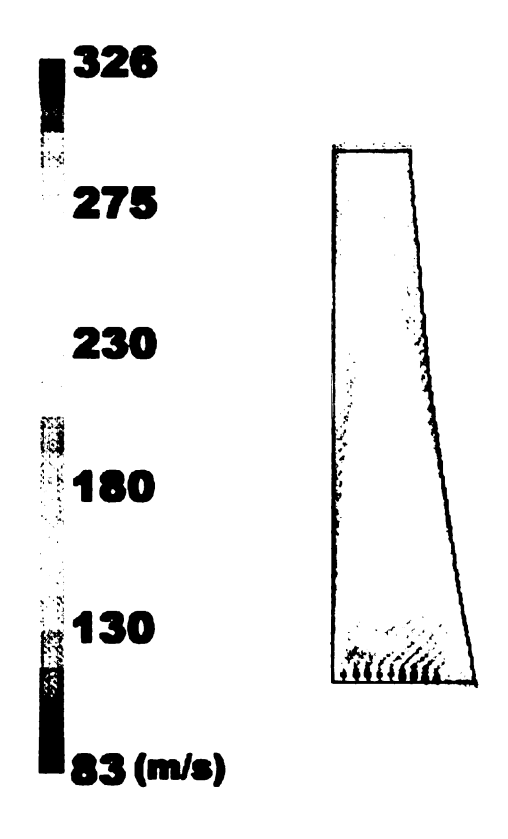


Figure 11-6: VELOCITY VECTORS COLORED BY VELOCITY MAGNITUDE

n = 20500 rpm

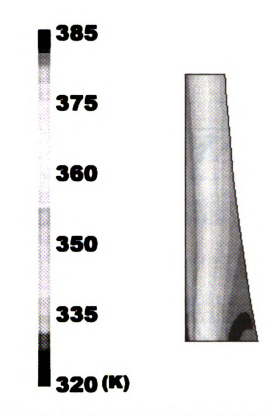
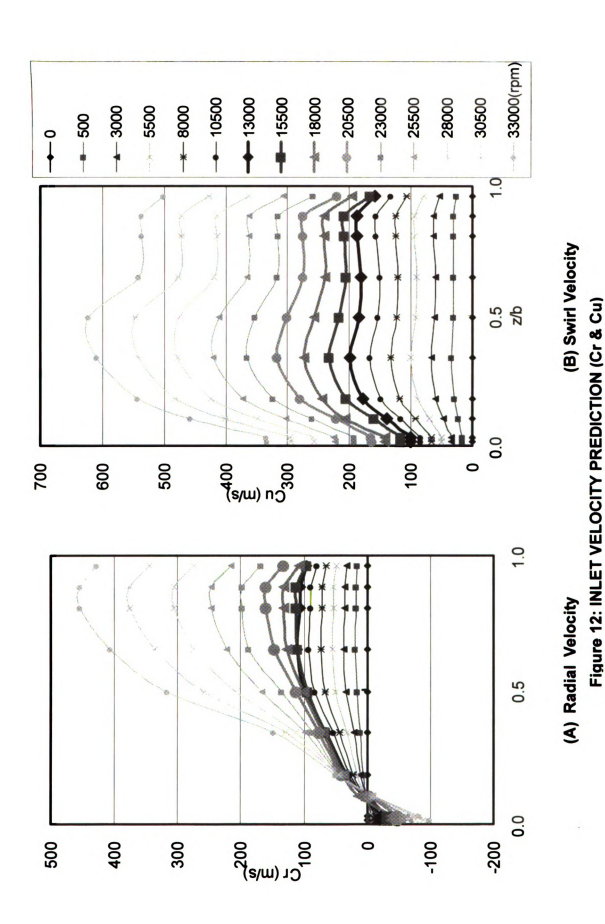
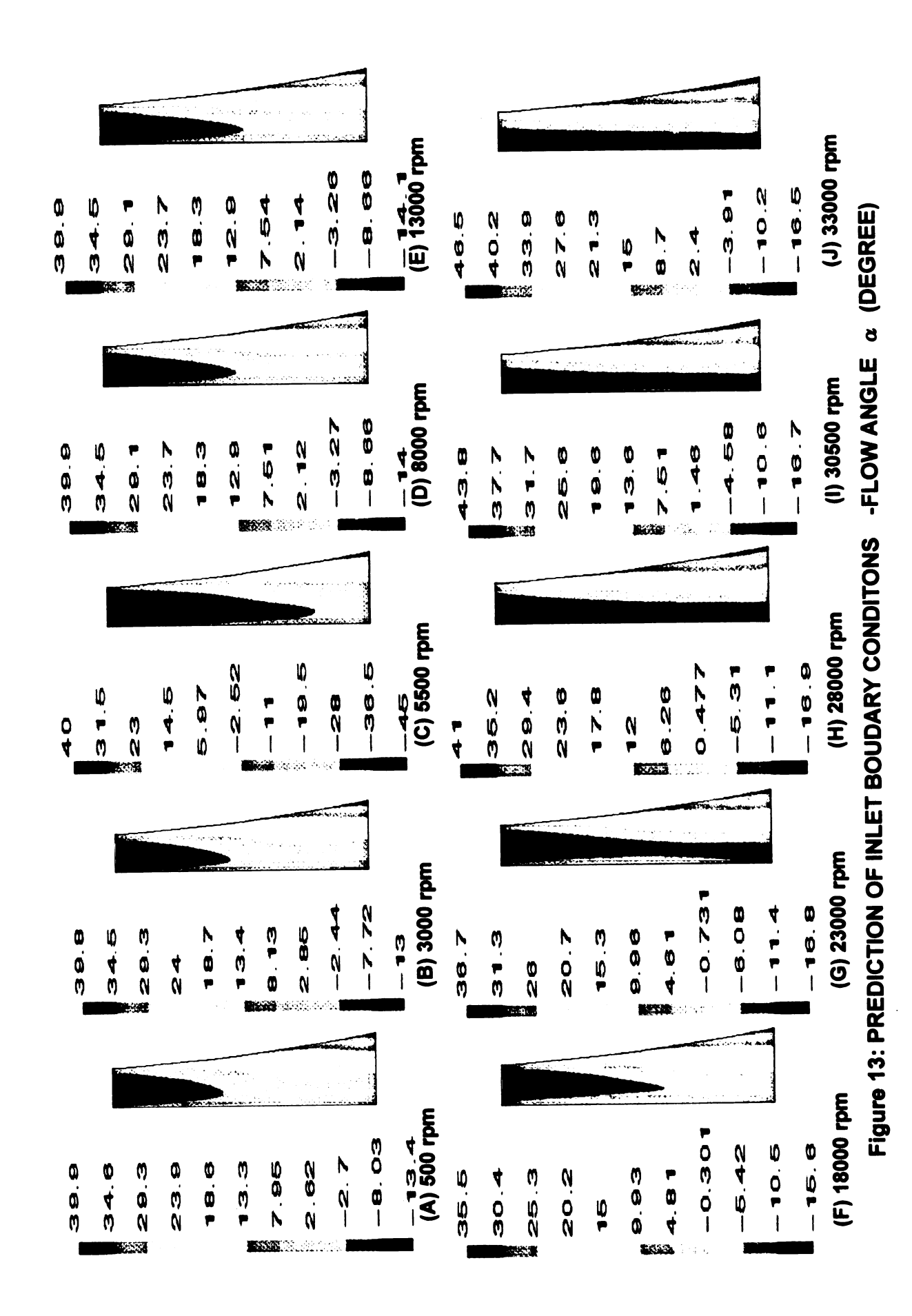


Figure 11-7: CONTOURS OF TOTAL TEMPERATURE (K)





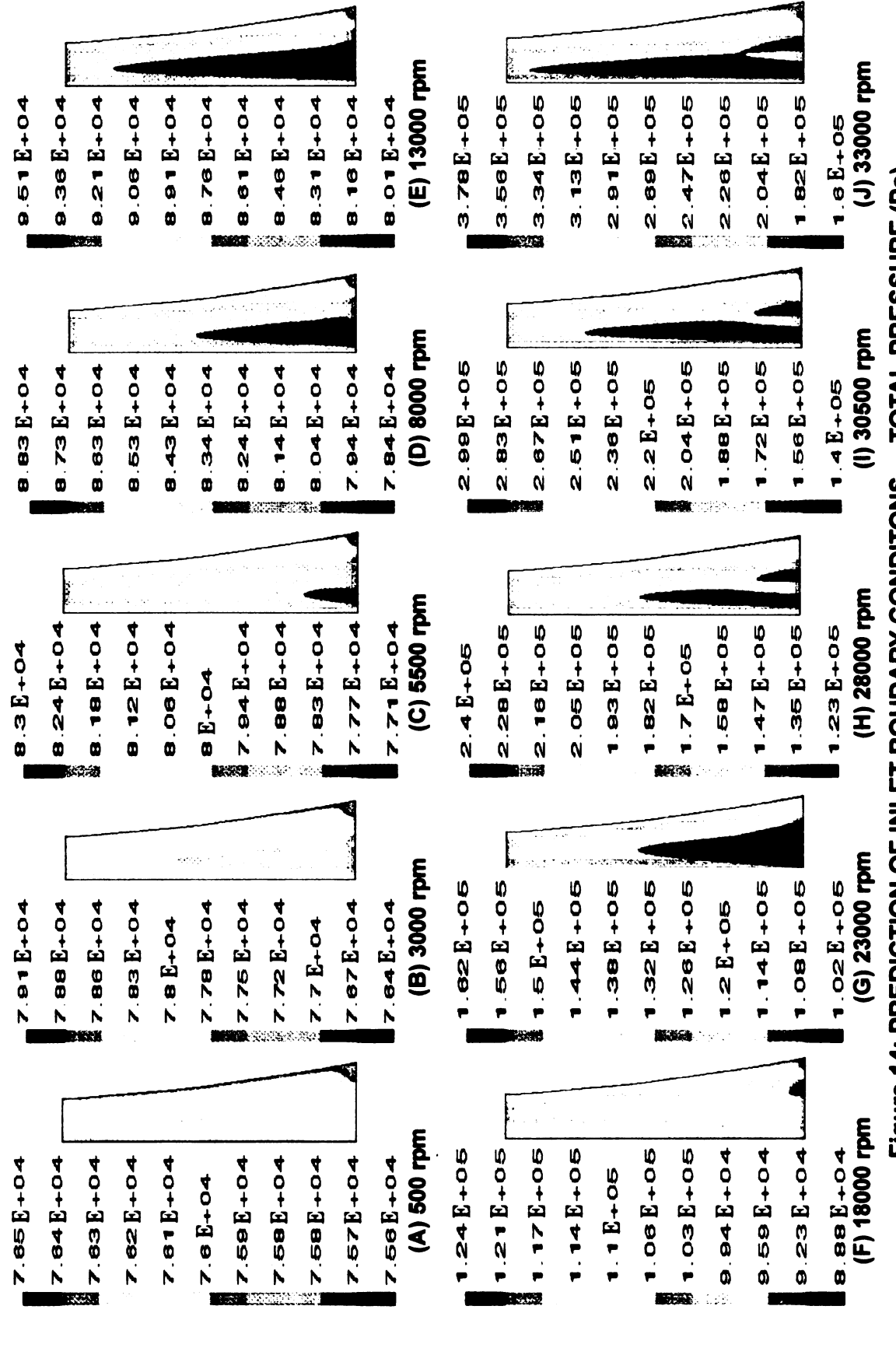
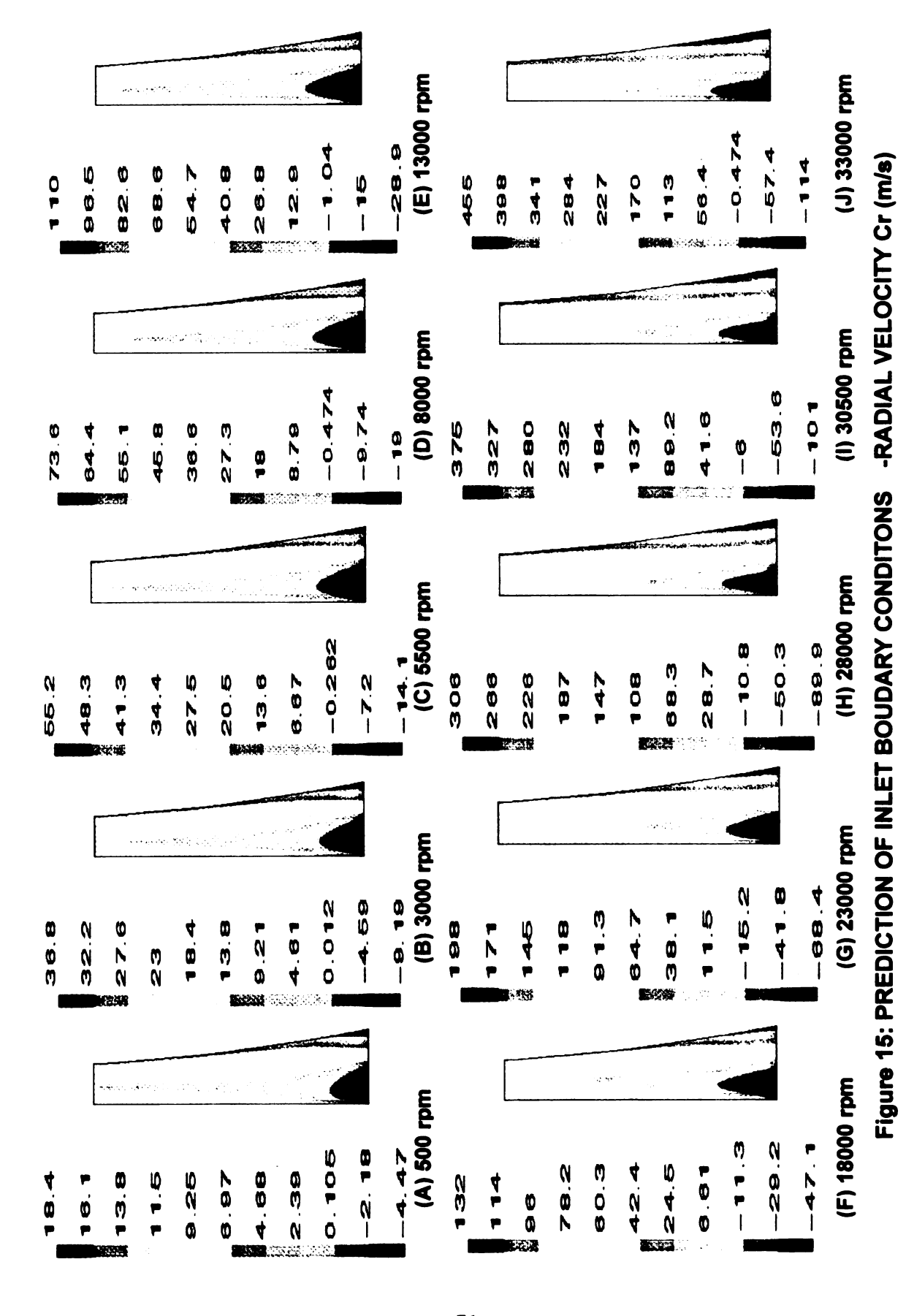
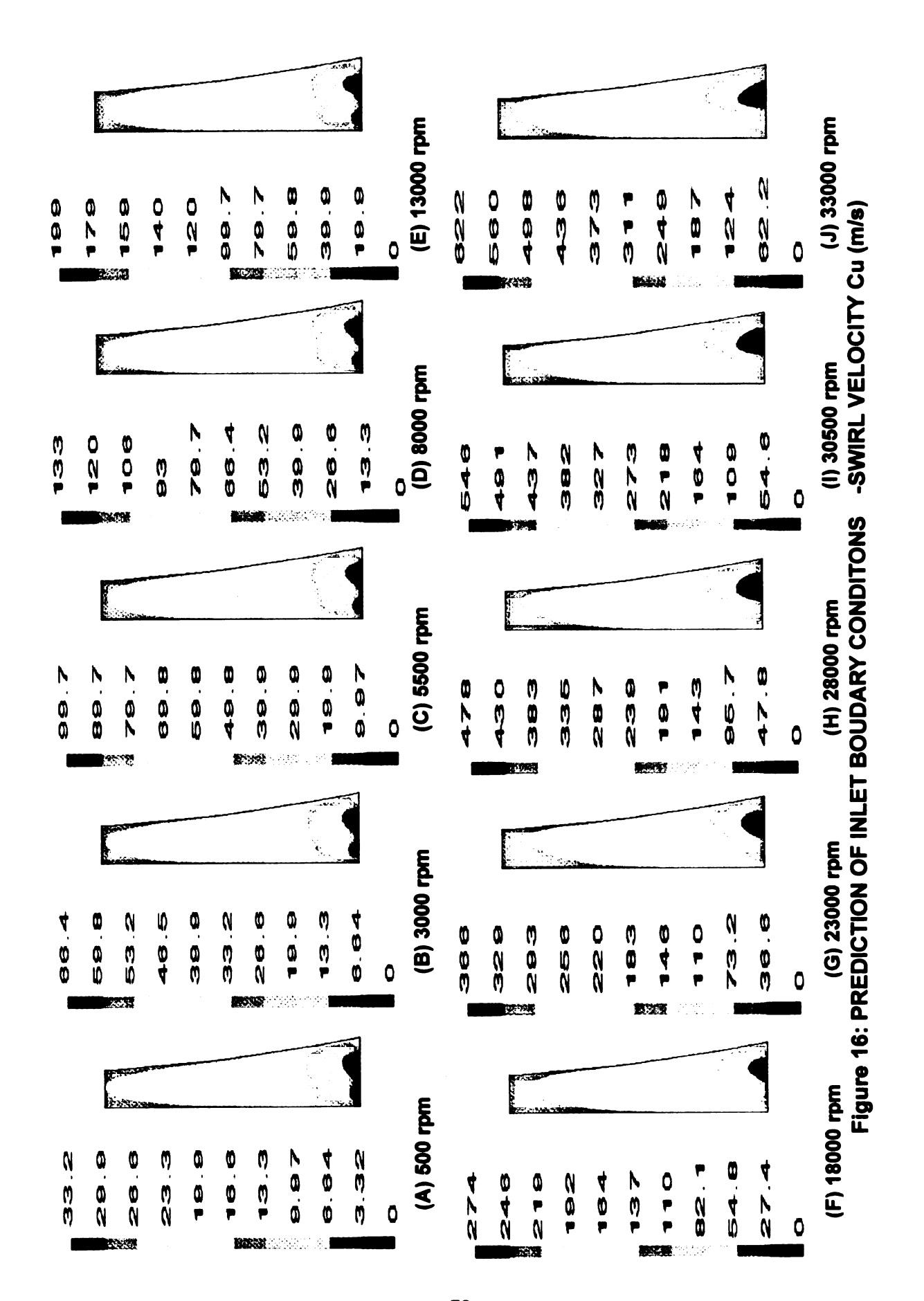


Figure 14: PREDICTION OF INLET BOUDARY CONDITONS -TOTAL PRESSURE (Pa)





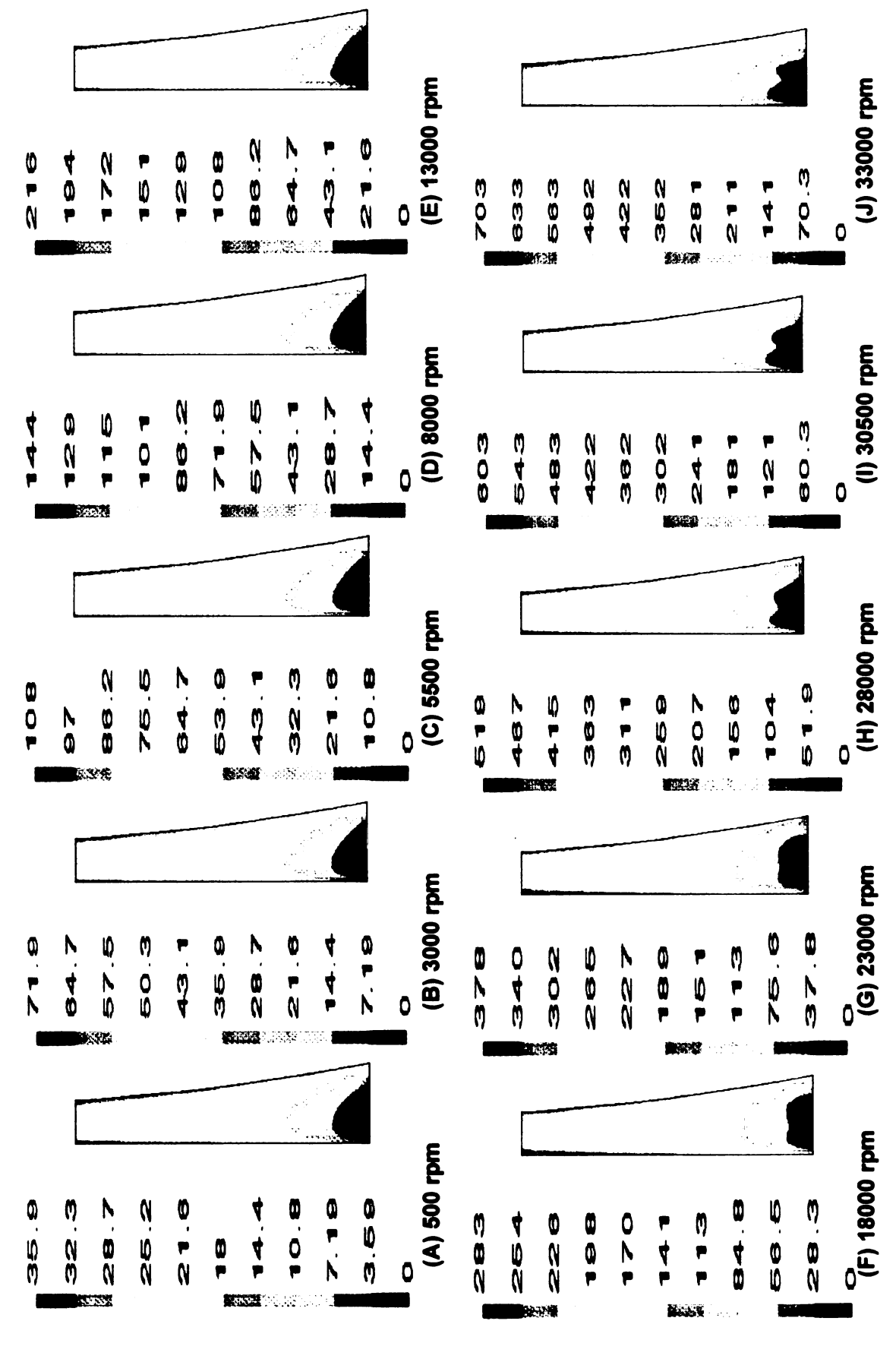


Figure 17: PREDICTION OF INLET BOUDARY CONDITONS -VELOCITY MAGNITUDE (m/s)

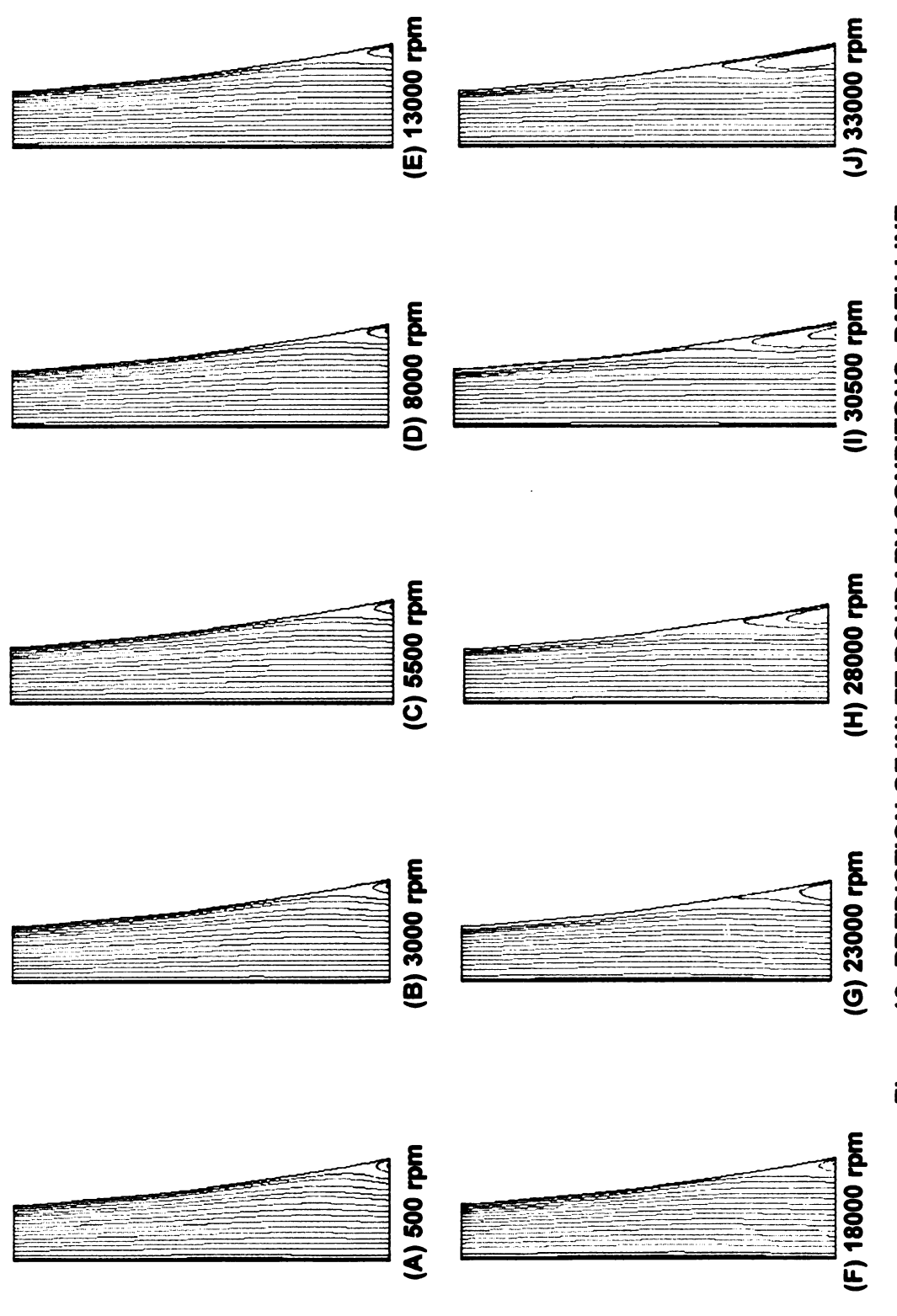


Figure 18: PREDICTION OF INLET BOUDARY CONDITONS -PATH LINE

